

LIMNOLOGY AND OCEANOGRAPHY

May 1995
Volume 40
Number 3

Limnol. Oceanogr., 40(3), 1995, 449–468
© 1995, by the American Society of Limnology and Oceanography, Inc.

Accumulation of marine snow at density discontinuities in the water column

Sally MacIntyre

Marine Science Institute, University of California, Santa Barbara 93106-6150

Alice L. Alldredge

Department of Biological Sciences, University of California, Santa Barbara

Chris C. Gotschalk

Marine Science Institute, University of California, Santa Barbara

Abstract

The vertical distribution of marine snow—aggregated particles >0.5 mm in diameter—was strongly correlated with density discontinuities in the upper 100 m of the water column at 33 stations off central California. Eighty-seven percent of peaks in aggregate abundance were associated with density discontinuities in which N^2 (the Brunt-Väisälä frequency) exceeded $1.25 \times 10^{-4} \text{ s}^{-2}$ ($N = 6$ cph). For 56% of the peaks, N^2 exceeded $2.5 \times 10^{-4} \text{ s}^{-2}$ ($N = 9$ cph). Absolute abundances of aggregates increased from a mean of 38.7 ± 18.3 aggregates liter $^{-1}$ above peaks to 59.3 ± 26.0 aggregates liter $^{-1}$ within peaks. Accumulations of aggregates could result from sinking into denser water if sinking rates were reduced by at least 20% due to slow equilibrium of either interstitial water or mucus within the flocs with the surrounding, higher density water. However, our observed increases in σ_t were insufficient to cause such slowing for flocs whose porosity was 99% or less; such flocs comprised a significant proportion of aggregates in the observed peaks. However, larger flocs of moderate to high porosity were likely to decelerate as they encountered denser water and could even become neutrally or negatively buoyant for changes in σ_t , such as we observed. Equilibration times of the interstitial water of these generally larger flocs ranged from hundreds of seconds up to 3 h. Results of a random walk simulation of particle motion indicated that turbulence was likely to cause localized accumulations of aggregates and to increase particle aggregation. Because we found subcritical values of the Richardson number (an indicator of turbulent mixing) at the top of regions of peak abundance but not at the base, for 68% of the peaks observed, we infer that turbulence may contribute to the accumulation of the smaller flocs. Occurrence of strong shear and deviations of temperature and salinity profiles from typical patterns suggest that at least 23% of these aggregate peaks were associated with horizontal intrusions.

Much of the suspended matter in the ocean exists as aggregates of microorganisms, inorganic particles, and detritus 0.5 mm or larger in diameter, known as marine snow. These aggregates harbor dense attached microbial

communities and serve as food for a variety of large particle-feeding zooplankton and fish (Alldredge and Silver 1988). They are enriched in nutrients (Shanks and Trent 1979) and sustain unique chemical microenvironments

Acknowledgments

We gratefully acknowledge the assistance of Sneed Collard, who developed the image processing software, Huamin Ma and Khai Trinh, who assisted with computer programming, the captains and crews of the RV *Pt. Sur* and *Spirit*, who assisted in innumerable ways, Bruce Dunson, who fabricated the camera frame, Mark Wendell, who assisted with the CAD software, and Orlando Sarnelle for advice on data analysis. The comments of J. M. Melack and two anonymous reviewers improved the

manuscript. J. C. Patterson provided his original version of the random walk model.

The work was funded by NSF grants OCE 92-16117 and OCE 89-22825 and ONR grant N00014-89-J3206 to A.L.A., through the Minerals and Management Service, U.S. Department of the Interior, under MMS Agreement 14-35-0001-30471 to S.M. and L. Washburn, and NSF grant DEB 93-17986 and ONR grant N00014-93-1-1001 to S.M.

within their interstices (Alldredge and Cohen 1987). Moreover, they are the major form in which particulate organic matter sinks to the ocean interior and the sea floor (Fowler and Knauer 1986).

The importance of marine snow to biological and chemical processes in the pelagic zone is significantly affected by its vertical distribution and abundance. Vertical accumulations or depletions of aggregates may affect the population sizes and trophic interactions of aggregate consumers and associated organisms, modify the magnitude of particulate flux at various depths, and alter the chemistry of the surrounding seawater, yet we know little about the vertical distributions of marine snow or the factors governing them, especially in surface waters. Previous studies with in situ photographic techniques have focused primarily on marine snow distributions at meso- and bathypelagic depths using sampling resolutions inadequate for uncovering the fine-scale variations appropriate for surface waters (Asper 1987; Asper et al. 1992; Gardner and Walsh 1990; Walsh and Gardner 1992; Davis and Pilskaln 1993). These studies report large variations in the abundance of marine snow in midwater, possibly as a result of episodic production in overlying waters, horizontal advection, or resuspension.

Stratification is ubiquitous in the upper ocean. Temperature, salinity, nutrients, oxygen, and algal and animal biomass are only a few of the parameters which show varying degrees of vertical stratification in the surface ocean. The intensity of turbulence also varies with depth. Turbulence is especially high in surface waters and may be elevated immediately above or within density discontinuities due to shear. Since aggregates are formed from coagulation processes related to the intensity of turbulent mixing and have settling rates sensitive to seawater density (Alldredge and Gotschalk 1988), marine snow would also be expected to vary in abundance depending on these factors and the concentration of component particles.

The following study was developed to investigate the fine-scale distribution of marine snow in surface waters (upper 100 m) and its relation to the vertical distribution of physical parameters. In particular, we examine the hypotheses that the vertical distribution of marine snow is significantly correlated with density gradients and intrusions and with turbulence in the water column.

Theoretical considerations

Turbulence is likely to lead to longer retention times (Alldredge et al. 1987) and to enhanced collision rates of particles. Its vertical distribution is not uniform and is related to vertical stratification in ways that depend on the mechanisms causing the turbulence. In the upper mixed layer, turbulence is caused by wind mixing and convective cooling; here, turbulence can be high where stratification is low. Within stratified portions of the water column, turbulence occurs due to shear caused by the tilting of internal waves or to internal wave interactions, both of which lead to shear instabilities. In fact, vertical shears are often highest where N^2 (Brunt-Väisälä fre-

quency squared, a measure of the change in density with depth) is largest (Carr et al. 1992; Peters et al. 1989). Mixing events, with accompanying overturns, can occur anywhere within the stratified waters, and their intensity, as measured by the rate of turbulent energy dissipation, ϵ , can be as high as or higher than in the wind-mixed zone (Padman and Dillon 1991). The likelihood of mixing by shear instabilities is determined by the Richardson number

$$Ri = -g/\rho(\partial\rho/\partial z)/(\partial u/\partial z)^2$$

where g is gravity, ρ is density, z is depth, and u is velocity. When $Ri < 0.25$, experimental studies have shown that Kelvin-Helmholtz instabilities develop and collapse into turbulent patches (Thorpe 1968, 1971).

The various theories and experiments used to determine this criterion for the development of Kelvin-Helmholtz instabilities are reviewed by Kundu and Beardsley (1991) who use their own data on temperature, shear, and wind events to verify the applicability of this criterion to the coastal ocean. The criterion that shear instabilities will develop when Ri is < 0.25 applies when density and shear are obtained from the localized region where the shear instability develops. Because of the logistics of oceanographic sampling, density and shear measurements are taken over larger scales than overturns, and the Ri so calculated is called the gradient Richardson number, Ri_g . Because overturns tend to be on scales of tens of centimeters to meters [with more on the small scales (Moum 1990; MacIntyre 1993; Wijesekera and Dillon 1991)] and because of the sampling problem, the existence of regions where Ri is less than critical may not be observed (Eriksen 1978; Padman and Jones 1985; Padman et al. 1990). Consequently, a less conservative value of the critical Ri may be needed, depending on the averaging scheme. Recent experiments in which turbulent microstructure, shear, and density stratification have been measured concurrently indicate that turbulence levels are elevated relative to the background levels when Ri_g is less than a critical value between 0.25 and 1 whose magnitude depends on the depth over which shear and N^2 were averaged (Carr et al. 1992; Yamazaki and Osborn 1993; Peters et al. 1989, 1991).

Although increases in density act to damp turbulence leading to abrupt decreases in ϵ at density discontinuities, increases in ϵ may also occur at the discontinuity because of enhanced shear. Weller et al. (1991) provided examples of these two different responses at temperature discontinuities; their data suggest that increases in ϵ are more likely at the more pronounced discontinuities. Imberger (1985), Padman and Dillon (1991), Gregg et al. (1993), and Yamazaki and Osborn (1993) all showed enhanced mixing just above or at the onset of a density discontinuity. Reasons for these increases within the discontinuity include the propagation of turbulent energy from an actively mixing region to a more quiescent one or to a combination of processes (Peters et al. 1989; Wijesekera and Dillon 1991; Itsweire et al. 1989).

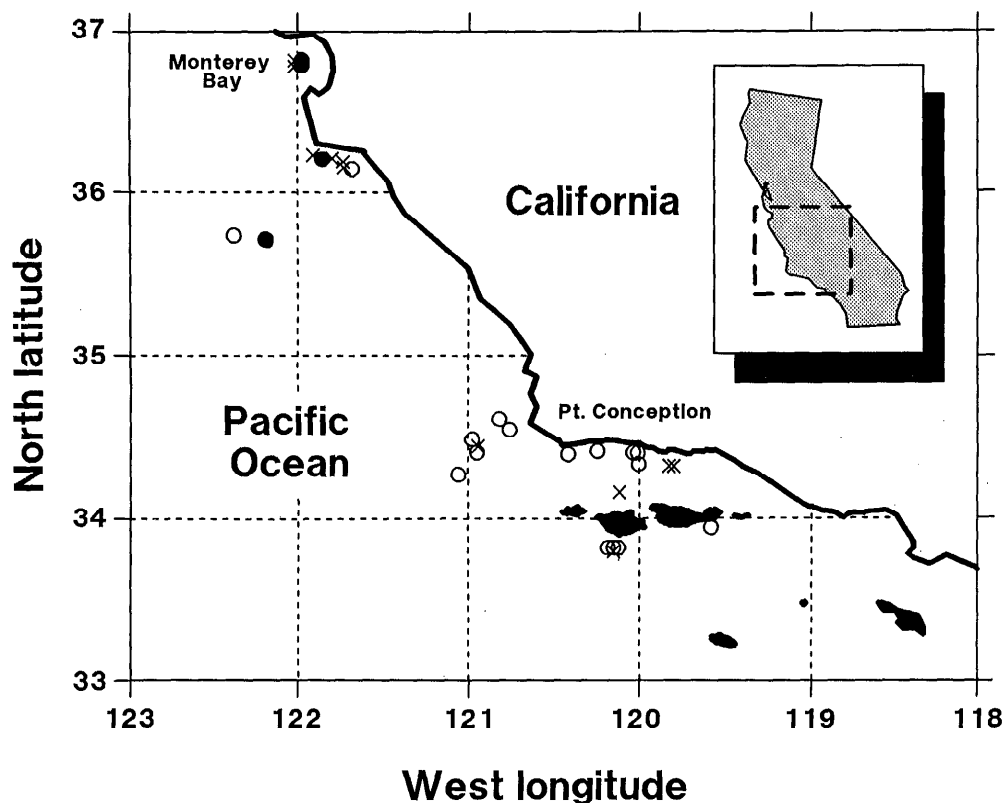


Fig. 1. Location of stations where vertical profiles of marine snow were obtained in April and May 1990–1992. Profiles were obtained during the day (0600–1880 hours—●), evening (2000–2200 hours—○), and at night (2400–0500 hours—×).

Methods

Field sampling—The vertical distribution of marine snow and hydrographic parameters in the upper 100 m of the water column was determined at 33 stations off central California in April and May 1990, 1991, and 1992 (Fig. 1) with a multi-instrument array containing a SeaBird CTD and two underwater camera systems (Fig. 2). Sixty percent of the stations were sampled in the early evening (2000–2200 hours), and the other 40% were sampled throughout the rest of the 24-h cycle. Marine snow collected by SCUBA divers throughout the study period by methods described by Alldredge (1991) was examined to determine the types of aggregates present at the stations.

Measurement of particle abundance and size—Vertical profiles of the abundance and size distribution of marine snow were obtained by photographing the aggregates present in slabs of illuminated seawater (0.78 liters in total volume) with either a still camera system or a video camera system, both modified from the design of Honjo et al. (1984).

The video system was used for all stations sampled in 1990 and consisted of a Pulnix TM740 black-and-white CCD video camera with a Pulnix 8 mm 1:1.3 C-mount lens and a Nikon UN-900 video camcorder, both in underwater housings. A slab of light normal to the camera

field of view was produced by 500 W of continuous light emanating from two 250-W halogen bulbs encased in an aluminum baffle and powered by a 24-V submersible battery. The beam was collimated as the light passed through three Fresnel lenses at the end of the baffle masked to produce a slab 5 cm thick (Fig. 2). The camera thus imaged a field $10.5 \times 14.7 \times 5$ cm. Depth, sensed with a pressure transducer, was encoded directly on each frame by a Pisces Video Encoder. Particle size was calibrated with a 5-cm-long wire permanently mounted horizontally midway in the light slab so it was visible at the top of each frame. Because the camera had a wide-angle lens, there was an apparent size difference for particles depending on their distance from the camera lens. Particles were sized assuming that they were all in the middle of the slab, yielding an accuracy for the diameter of $\pm 15\%$.

The video system produced large numbers of continuously generated frames and provided a large data set. Its resolution at the frame size used, however, was only $250 \mu\text{m}$ per pixel. We counted only particles which were at least 2 pixels, or 0.5 mm, in size. $f/3$ gave accurate size and abundance information for translucent reference particles (smelt eggs) calibrated in a laboratory tank. Larger f -stops underestimated particle number, while smaller ones overexposed particles and increased their apparent size. An exposure time of $1/250$ s provided maximum light with no ghosting effects from the heaving of the ship.

The still camera system consisted of a Photosea 5000

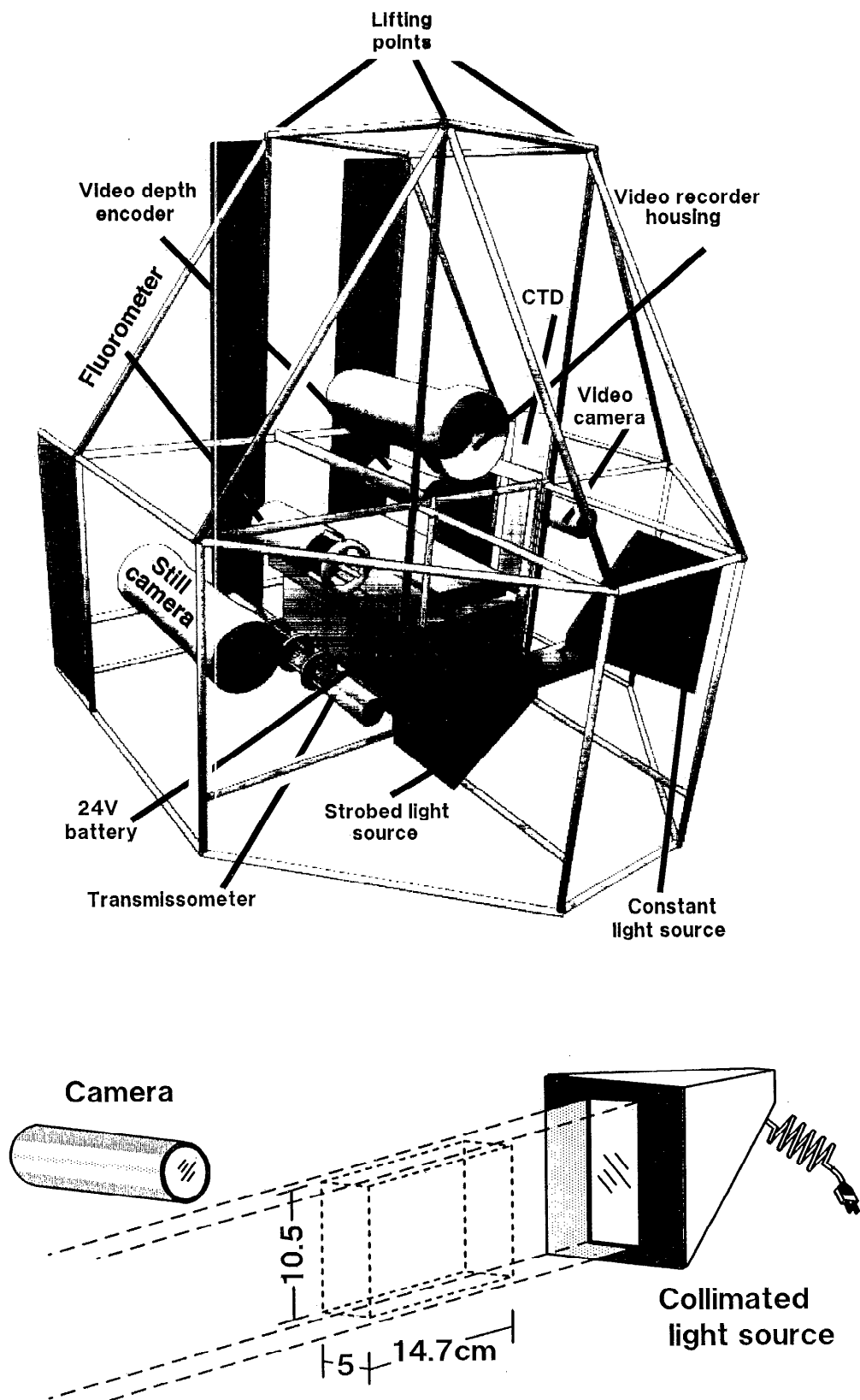


Fig. 2. Instrument package used to obtain two-dimensional profiles of aggregate abundance and water-column hydrography. Above. Diagram of the entire package equipped with both a video and a still camera, CTD, fluorometer, and transmissometer. Lights and cameras were powered by a 24-V battery. The vertical fins at the rear of the package orient the cameras into any apparent

35-mm camera with a 55-mm Nikon macrolens and a Photosea 1500S strobe in a collimating baffle similar to that of the video camera. The camera was set at $f/16$ and synchronized with the strobe, which had a 0.001-s flash duration and an output of 150 W s^{-1} . Photographs were taken at 10-s intervals to allow time for the strobe to recycle and avoid overheating. The lens port was a flat glass plate that nearly eliminated the distortion in size of particles at different distances from the lens.

Photographs of collimated slabs of light $10.5 \times 14.7 \times 5 \text{ cm}$ were recorded on T-max 400 black-and-white film (800-exposure rolls). Two sampling strategies were used. At some stations, the camera was stopped at 2-m intervals to 100 m, and 6 replicate photographs were taken at each stop. At others, the camera was lowered slowly but continuously ($4\text{--}6 \text{ m min}^{-1}$). The two strategies yielded the same total number of photographs per profile ($\sim 250\text{--}300$). Frame number and time of exposure were recorded on each frame and matched to the corresponding CTD depth. The still camera produced fewer frames for analysis but had a much higher resolution than the video camera. A resolution of $35 \mu\text{m}$ was achieved, limited by the 1,000-line video camera used during image analysis of the developed negatives. However, only particles $\sim 500 \mu\text{m}$ are reported here.

Oblique hauls to 100 m with a meter net ($333\text{-}\mu\text{m}$ mesh) carried out at most stations indicated that $<1\%$ of the particles observed by our camera system were zooplankton.

Image analysis of aggregates—Particle sizes and abundances were quantified from both video and still camera outputs with a Megavision 1024 XM image analysis system. Eight-millimeter videotapes were transferred to VHS on a Hitachi VCR UT-F3XA so they would be in the appropriate format for analysis by the computer. Each 35-mm exposure on the still camera negatives was scanned with a 1,000-line Megavision video camera fitted with a 50-mm AF Nikor 1:1.8 lens, and this video output was analyzed by the computer. Thresholding was set visually at the beginning of each videotape or for each individual frame on the still film. Background sunlight interfered with the imaging of particles in the upper 5–7 m for a few profiles taken during the day. These depths were excluded from analysis on these profiles.

Particle abundances were smoothed, either with a 5-point Hanning filter, for profiles taken continuously, or with a 9-point Hanning filter for those taken at 2-m intervals. Interpolation of particle abundances to 0.5-m intervals for later data analysis was done with a cubic spline procedure (deBoor 1978). The rate of change in aggregate abundance with depth (dP/dz) was calculated with data weighted following Patterson (1983).

Density profiles—All camera profiles were accompanied by simultaneous profiles of temperature and conductivity sampled at a frequency of 2 Hz with a SeaBird SBE19 CTD. Salinity and density were computed from these data using the equation of state of seawater (Fofonoff and Millard 1983). To reduce spiking (the artificially induced increase in calculated salinity and density due to the differences in the depth of measurement caused by the different physical locations of the sensors and the mismatch in their time constants, Fozdar et al. 1985), we aligned temperature and conductivity signals relative to pressure and delayed conductivity measurements 0.25 s while advancing temperature measurements 0.4 s. Brunt-Väisälä frequencies, $N^2 = -g/\rho(\partial\rho/\partial z)$, were calculated by obtaining $\partial\rho/\partial z$ (the change in density with depth) by differencing over three depth intervals following Patterson (1983). The data were then Hanning filtered with either a 5- or 9-point filter chosen to match the sampling scheme for the particle or acoustic Doppler data (see below).

Temperature and conductivity data were also sampled at a few stations with a free-falling CTD that sampled every 3 mm (Ocean Sensors model 100 CTD). To reduce spiking, we sharpened and smoothed the raw signals from this instrument according to Fozdar et al. (1985). Salinity and density were computed as described above.

Current velocities and Richardson numbers—Current speed and direction were measured in 4-m bins with an RD Instruments 150 kHz, hull-mounted acoustic Doppler current profiler (ADCP) at 15 of the 33 stations examined. All data were processed with bottom tracking to remove the ship's velocity from the measured velocity. Shear magnitude was calculated from the center of one bin to the center of the next as

$$\partial u/\partial z = [(\partial u_i/\partial z)^2 + (\partial u_j/\partial z)^2]^{1/2}$$

where u_i and u_j are the northerly and easterly components of velocity.

Richardson numbers were calculated from Brunt-Väisälä frequencies (N^2) and shear stresses. To calculate N^2 for the estimates of Ri , we first smoothed the density profiles with a 9-point Hanning filter, computed N^2 where the density differences were obtained using differences weighted over three successive depths (Patterson 1983), and then smoothed the resulting N^2 values again with a 9-point Hanning filter. Because the density data were obtained at 0.5-m intervals, the 9-point Hanning filter effectively smooths over 4-m bins to correspond to the sampling interval for the Doppler data. The depths of the Doppler data and of N^2 were matched with a cubic spline interpolation (deBoor 1978). The interpolation of the shear values from the center of each bin assumes a smooth

current. Below. Lighting technique for both the video (continuous) and still (strobed) cameras. Each light source was passed through a sandwich of three Fresnel lenses producing a collimated beam 5 cm thick. The camera was positioned perpendicular to the beam and imaged only the aggregates illuminated within the beam.

change in shear. We examined the interpolated data to make sure shear was not over- or underestimated. If it was, we recalculated Ri based on the measured values of shear.

Because our profiles of density and velocity were averaged over 4-m scales and our observations with the fine-structure CTD (not shown) showed overturns to be on scales of tens of centimeters, we assume that localized mixing events occur wherever $Ri \leq 1$.

Criteria for identifying accumulations of particles—We defined peaks in particle abundance based on at least a 25% increase in maximum particle abundance relative to the abundance of aggregates averaged over the three depths immediately above the depth at which abundance began to increase. We determined where these peaks occurred in relation to regions with moderate and large changes in density ($N^2 \geq 1.25 \times 10^{-4} \text{ s}^{-2}$ and $2.5 \times 10^{-4} \text{ s}^{-2}$, respectively), with enhanced shear, and relative to $Ri \leq 1$.

We noticed that increases in particle abundance of lesser magnitude were present, and these increases also co-occurred with hydrographic features. These increases were not large enough to justify calling them peaks. Consequently, we used the derivative of particle concentration with respect to depth as a sensitive measure to identify where these increases occurred as well as to identify increases in particle abundance in well-defined peaks. We defined as significant an increase of $dP/dz \geq 1$ aggregate $\text{liter}^{-1} \text{ m}^{-1}$. We determined where these increases occurred relative to density discontinuities (with $N^2 \geq 1.25 \times 10^{-4} \text{ s}^{-2}$) as well as to changes in salinity and the value of the Richardson number.

Results

Although all 33 stations were investigated in April and May, there was considerable variability in hydrography and the composition of marine snow from station to station both over the 3-yr span of the study and within any given year. Aggregates formed primarily of diatoms, especially *Nitzschia* spp. and *Chaetoceros* spp., often with incorporated macrocrustacean fecal pellets, occurred at about half the stations in 1990 and 1992. Discarded larvacean houses and aggregates dominated by macrocrustacean fecal pellets and miscellaneous detritus dominated the rest of these stations and the stations sampled in 1991.

The degree of stratification of the upper 100 m of the water column also varied considerably. Of the 33 stations examined, 27% could be considered two-layered systems with well-mixed upper layers, strongly stratified (defined as $>3^\circ\text{C}$ change) thermoclines, and well-mixed water below, and 6% were two-layered systems with weakly stratified thermoclines. The water column was linearly stratified with no upper mixed layer at 27% of the stations, was linearly stratified with a shallow (4–10 m) upper mixed layer at 21% of the stations, and was linearly stratified with an upper mixed layer 10–35 m deep at 16% of the stations. Only one station (3% of stations) was nearly isothermal in the upper 100 m. Stratification and shears

were comparable to those obtained over the continental shelf in northern California and in Monterey Bay in springtime (Kundu and Beardsley 1991; Yamazaki and Osborn 1993).

Association of aggregate abundance with regions of high Brunt-Väisälä frequency—Peaks in aggregate abundance were strongly associated with density discontinuities, indicated by large values of N^2 , at all the stations investigated. Figure 3 illustrates these relations. The water column at this station was two-layered with a prominent pycnocline from 15 to 24 m (Fig. 3A). N^2 reached a maximum of 0.0015 s^{-2} at 20 m (Fig. 3B). Increased σ_t resulted primarily from decreases in temperature since salinity changed little in the pycnocline region (not shown). The abundance of aggregates with an equivalent spherical diameter $>0.5 \text{ mm}$ increased in the pycnocline, reaching a maximum at a depth corresponding exactly to the depth of maximum N^2 (Fig. 3A,B). Abundance of aggregates in this peak increased by 52% over aggregate abundances in the mixed layer directly above the peak. The maximum rate of increase in particle abundance, however, occurred 2–3 m above the depth of maximum aggregate abundance and of maximum N^2 (Fig. 3B).

The mean volume of individual aggregates was greatest at 29 m, $\sim 10 \text{ m}$ below the depth of maximum aggregate abundance (Fig. 3C). Because larger, although fewer, aggregates were found slightly below the peak in aggregate abundance, the total cumulative aggregate volume also reached a maximum several meters below the maximum N^2 (Fig. 3).

N^2 also exceeded $1.25 \times 10^{-4} \text{ s}^{-2}$ at 30, 40–44, 54, 84, and 94 m (Fig. 3B). As shown below, increases in aggregate abundance were associated with these moderate density changes $\sim 50\%$ of the time. In this case, dP/dz is ≥ 1 aggregate $\text{liter}^{-1} \text{ m}^{-1}$ only between 40–46 m (Fig. 3B).

A summary of analyses comparable to that described for Fig. 3 but for all 33 stations is presented in Table 1. The data are grouped by criteria for defining peaks and increases in aggregate abundance. The vast majority of increases in aggregate abundance which met our threshold criteria were associated with density discontinuities. Of the 54 identified aggregate peaks, 87% were within 4 m of a moderate density discontinuity ($N^2 \geq 1.25 \times 10^{-4} \text{ s}^{-2}$), and 56% were within 4 m of a strong density discontinuity ($N^2 \geq 2.5 \times 10^{-4} \text{ s}^{-2}$). Of the 146 increases in abundance defined by $dP/dz \geq 1$ aggregate $\text{liter}^{-1} \text{ m}^{-1}$, 84% were at density discontinuities where N^2 was $\geq 1.25 \times 10^{-4} \text{ s}^{-2}$. Moreover, the aggregate maxima was located within 2 m of the maximum N^2 for 85% of particle peaks and was similarly located for 80% of significant particle increases. Of the remaining cases, aggregate abundance peaks were about equally distributed above or below the maximum N^2 (Table 1).

The maximum rate of increase in aggregate number (Fig. 3B) was as likely to be 2–4 m above a density discontinuity as within it, whereas the depth of maximum aggregate abundance usually was within 2 m of the maximum N^2 (Table 1). This pattern is illustrated by peaks

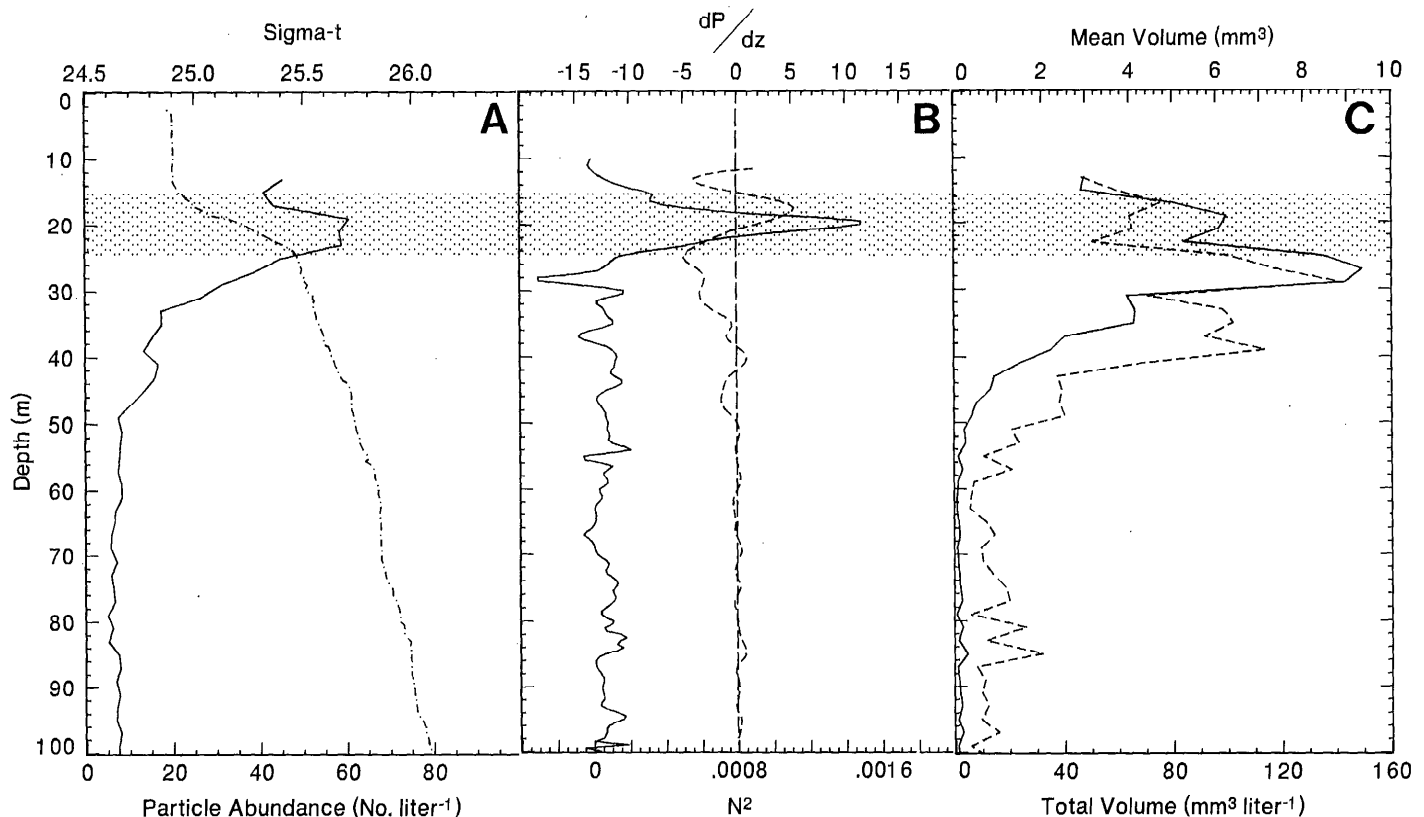


Fig. 3. Example of data collected at a typical station (18 April 1990, 2200 hours; 33°48'N, 120°8'W). Shaded area denotes the depth region where a peak in aggregate abundance (defined as >25% increase in absolute abundance of number of aggregates compared with abundance directly above the area of increase) occurred and is shown to help focus attention across the panels. Shading begins at the depth where aggregate concentrations are increasing ($dP/dz > 0$, panel B) and ends at the depth where aggregate concentration decreases at its maximum rate. A. Vertical profile of σ_t (---) (kg m^{-3}) and aggregate abundance (—). Data on particle abundance were obtained with the video camera. B. Vertical profiles of Brunt-Väisälä frequency, N^2 (s^{-2}) (—) and derivative of particle abundance with respect to depth, dP/dz (---). Threshold for discriminating increases in particle abundance was $dP/dz \geq 1 \text{ agg. liter}^{-1} \text{ m}^{-1}$. Vertical line indicates where dP/dz equaled 0. C. Mean volume of individual aggregates (---) and total cumulative volume (—) of aggregates in the water column. This station had relatively large aggregates.

1, 3, and 5 in Fig. 4A,B and in peaks 1 and 2 in Fig. 5 (shaded areas). In these examples, particles began to accumulate where the water column was weakly stratified or decreasing in stratification. Where the rate of increase in the particle abundance was maximum, N^2 values were still near zero. Not until particle abundances were maximum (dP/dz returned to zero) did N^2 values increase to near maximum values, generally above $1.25 \times 10^{-4} \text{ s}^{-2}$.

Peak 2 (Fig. 4A) does not follow the general pattern documented in Table 1. Although it did begin where stratification was minimal and stratification did increase within the region of the peak, the maximum dP/dz was >6 m above strongly stratified waters, and N^2 was $<1 \times 10^{-4} \text{ s}^{-2}$ at the particle maximum (Fig. 4B). It will be seen later that this peak was due to an intrusion.

Aggregates tend to be more abundant in more highly stratified waters and to increase in abundance more rapidly as N^2 increases (Fig. 6A,B). Since the maximum in dP/dz occurs 2–4 m above the maximum in N^2 , it may not be that stratification itself directly affects the rate of particle increase but rather that the increased shears are

commonly associated with regions with higher N^2 (Carr et al. 1992; Peters et al. 1991).

Most peaks in aggregate abundance occurred at density discontinuities, but not all density discontinuities had increases in aggregate abundance associated with them. Only 47% of the 187 discontinuities defined by $N^2 > 1.25 \times 10^{-4} \text{ s}^{-2}$ had associated significant increases in dP/dz , and only 25% had associated particle peaks (Table 1). Our data indicate that while the existence of an aggregate peak generally predicts an associated discontinuity, the reverse is less likely. Where density discontinuities occur without peaks in aggregate abundance, the particles from which aggregates are formed or the organisms which contribute to the production of marine snow may not be present.

We examined variations in mean aggregate size, determined as mean aggregate volume, and total cumulative aggregate volume with depth for the 54 peaks in aggregate abundance (Table 1). Of these peaks, 66% also displayed associated increases in mean aggregate size. Of these 36 abundance peaks, only 10% had the largest mean aggre-

Table 1. Association between increases in aggregate abundance and the vertical positions of density discontinuities.

	Subtle and pronounced increases ($dP/dz > 1$)	Pronounced peaks (increase in aggregate abundance > 25%)
	$N^2 > 1.25 \times 10^{-4} \text{ s}^{-2}$	
Profiles examined	33	33
Density discontinuities	187	187
Increases in aggregates	146	54
Increases in aggregates associated with discontinuities	123	47
% of discontinuities with associated increases in aggregates	47	25
% of increases in aggregates occurring at discontinuities	84	87*
% of aggregates abundance increases with associated increases in aggregate size	—	66
Aggregate increases associated with discontinuities		
Position of maximum in abundance relative to discontinuity		
% 2–4 m above	10	9
% in (correspond ± 2 m)	80	85
% 2–4 m below	10	6
Position of maximum rate of particle increase relative to discontinuity		
% 2–4 m above	48	53
% in (correspond ± 2 m)	52	45
% 2–4 m below	0	2
Abundance peaks with associated increases in aggregate size		
% of size peaks above abundance peak	—	10
% of size peaks in abundance peak (± 2 m)	—	32
% of size peaks below abundance peaks	—	58
Mean distance of size peaks above abundance peak (m)	—	5.0 ± 0.5
Mean distance of size peaks below abundance peak (m)	—	7.0 ± 2.4

* 56% occurred where $N^2 > 2.5 \times 10^{-4} \text{ s}^{-2}$.

gate size occurring an average of 5.0 ± 0.5 m above the depth of maximum aggregate abundance peak, while 58% had the maximum aggregate size an average of 7.0 ± 2.4 m below the depth of maximum aggregate abundance (Figs. 3C, 4D—peak 2), suggesting that aggregates were differentially distributed by size within the range of each abundance maximum.

Although maximum aggregate size was often below peaks in aggregate abundance, vertical patterns in total cumulative aggregate volume were nearly identical to those of total abundance in all the profiles examined (see Figs. 3C, 4D, 5D). This concordance was largely because aggregates in the size range of 0.5–1 mm in diameter made up >90% of the aggregates present at most stations and made up a large portion of the total cumulative aggregate volume.

Table 2 contains a summary of the absolute abundances and sizes of aggregates associated with abundance peaks. These data indicate that significantly more and larger aggregates occur in association with density discontinuities than in isopycnal areas above these discontinuities.

Aggregate abundance increased by an average of 20.6 ± 19.1 aggregates liter⁻¹, averaging 58% higher in the abundance peak than above it. Aggregate abundances in all the peaks ranged from 6 to 110 aggregates liter⁻¹. Aggregate size also increased from a mean diameter of 1.1 mm above each peak to 1.6 mm in it. Aggregate size above each peak was calculated as the average mean aggregate size at the three depths directly above the depth at which aggregate abundance began to increase. Total volume of aggregates >0.5 mm increased by 123% from a mean of 43 mm³ liter⁻¹ above the peaks to 95 mm³ liter⁻¹ at the abundance maximum.

The range of particle sizes was quite large within particle peaks. For instance, when the mean aggregate diameter was 2.7 mm, the range of particle sizes in the peak spanned 0.5–10-mm diameter.

Current shear, changing hydrography, Richardson's number, and particle abundances—Shear due to changes in current speed and direction with depth, horizontal intrusions, and turbulent mixing can all influence the ver-

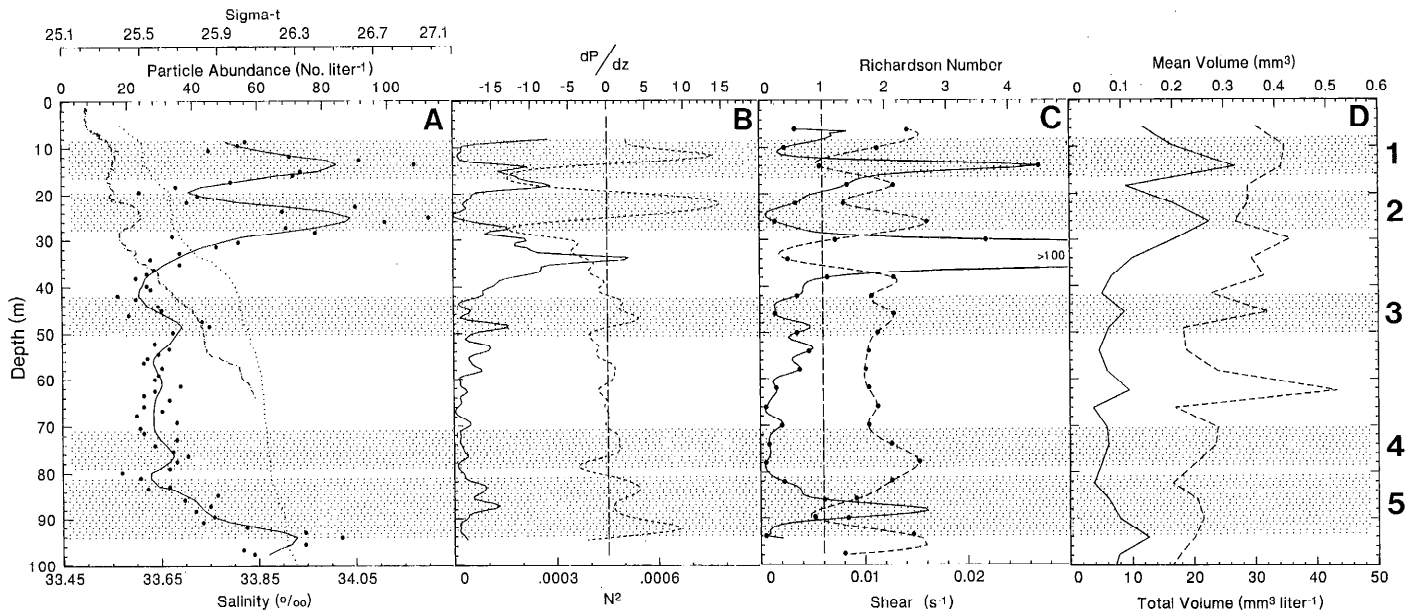


Fig. 4. Profiles of station 41 (29 April 1991, 0600 hours; 34°21'N, 119°52'W). Shading as in Fig. 3. A. Vertical profile of σ_t (.....) (kg m^{-3}), aggregate abundance (—), and salinity (---). Salinity was measured with the fine-structure profiler. B. As panel B of Fig. 3. C. Current shear (-----) and Richardson number, Ri (—). Turbulent mixing was likely for $\text{Ri} \leq 1$. Dashed vertical line is at $\text{Ri} = 1$. We used the criterion $\text{Ri} \leq 1$ to infer the likelihood of turbulent mixing because Ri was calculated from N^2 and shear² averaged over 4-m depths, an averaging scale considerably larger than the ~40-cm overturns we observed. D. As panel C of Fig. 3.

tical distribution of particles with depth. ADCP data obtained at 15 of our stations provide information with which to estimate the importance of these processes on the vertical distribution of aggregates.

The aggregate peaks in Figs. 4 and 5 show three patterns with respect to shear. In the first pattern, peaks were

pronounced where mean shears were initially relatively high and then decreased; N^2 was inversely correlated with shear (peaks 1 and 5 in Fig. 4, all peaks in Fig. 5). We will explore the relation of shear and density using the Richardson number—the ratio of N^2 to shear squared. In the second pattern, high mean shears were associated with

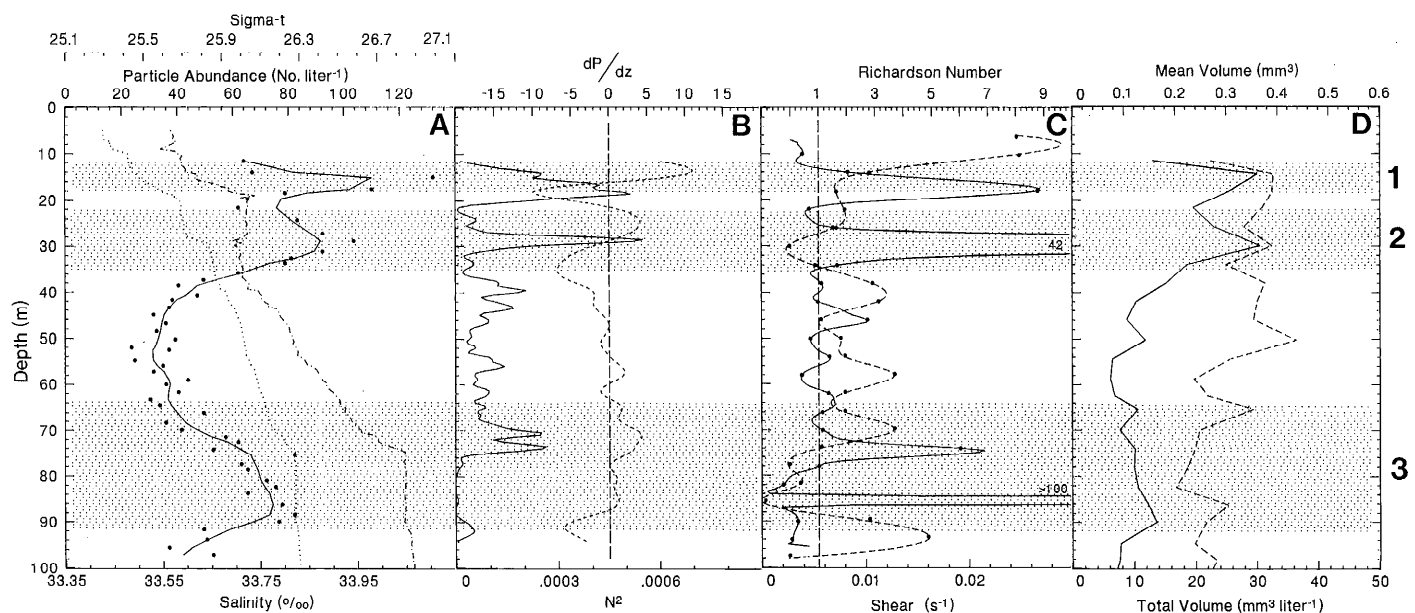


Fig. 5. Profiles of station 42 (29 April 1991, 1200 hours; 34°21'N, 119°52'W). All panels as in Fig. 4, except salinity was measured by the SeaBird CTD.

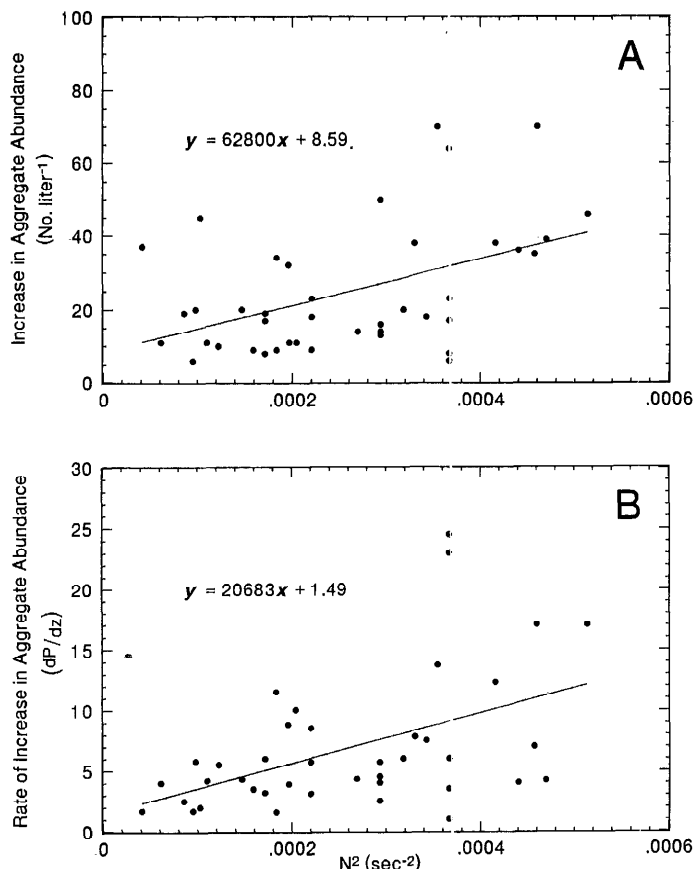


Fig. 6. Increase in aggregate abundance with increasing Brunt-Väisälä frequency. A. Increase in absolute aggregate abundance in particle peaks relative to abundance directly above the peaks vs. N^2 ($r^2 = 0.33$; $P < 0.0004$). B. Rate of increase in aggregate abundance (dP/dz) vs. N^2 ($r^2 = 0.16$; $P < 0.019$).

peaks with smaller percent increases in particle abundance (peaks 3 and 4 in Fig. 4). Clearly it is not high mean shears alone that lead to large particle accumulations. In the third pattern, increases in shear are associated with hydrographic changes, and the combination suggests horizontal intrusions may have brought particles into a region (peak 2 in Fig. 4).

By looking at the hydrographic data for the profiles for which ADCP data were available, we were able to assess the frequency of intrusions. Thirty-five percent of the

Table 3. Particle peaks, intrusions, and Richardson number.

	Particle increase in abundance > 25%
Number of profiles examined	15
particle abundance peaks	31
Number of particle abundance peaks with marked changes in speed or direction	11 (35%)
changes in T or S suggestive of intrusion	9 (29%)
both velocity and T or S suggestive of intrusions	7 (23%)
$Ri \leq 1$	30 (97%)
$Ri \leq 1$ near top of peak	24 (77%)
$Ri \leq 1$ near top of peak and > 1 below	21 (68%)

particle peaks were associated with marked changes in speed or direction of currents (shear). Twenty-nine percent were associated with sudden decreases in salinity, increases in temperature at depth, or near-isothermal or isohaline regions co-occurring where the waters had previously been gradually changing in properties (Table 3). Changes in velocity and hydrographic properties co-occurred 23% of the time. Although these features do not definitively indicate intrusions of particle-rich water, their co-occurrence does provide evidence of intrusions and may account for at least 23% of the particle peaks.

Peak 2 of Fig. 4 is an example of particle accumulations likely to have been caused by an intrusion. Where particle abundances were high, shear increased and was as large as observed in our study. The salinity profile taken concurrently indicated high-salinity water overlying lower salinity water in the region of the peak. Data from the fine-structure CTD taken half an hour before the cast (Fig. 4A) and 4 h later clearly show an intrusion of lower salinity water between 22 and 29 m.

Richardson numbers and particle abundances—At least 97% of the time, peaks in particle abundance were associated with $Ri \leq 1$ (Table 3). Since $\sim 50\%$ of the water column in each of the profiles has $Ri \leq 1$ and many of these regions are not associated with increases in particle abundance, mixing by itself was not sufficient to cause appreciable accumulations. However, just as with the

Table 2. Mean aggregate abundance and size above and within aggregate peaks (peak defined as increase in abundance $> 25\%$). Data obtained with still camera.

	Mean aggregate abundance (No. liter $^{-1}$)	Mean aggregate diam. (mm)	Total cumulative aggregate vol. (mm 3 liter $^{-1}$)
Above peak	38.7 \pm 18.3	1.1 \pm 1.2	42.6
In peak maximum	59.3 \pm 26.0	1.6 \pm 2.3	94.9
Absolute increase	20.6 \pm 19.1	0.5 \pm 0.7	52.3
Means % increase in peak	58%	55%	123%
Range of means in peak	6–110	0.7–4.1	11–350

Table 4. The number of times Richardson numbers were ≤ 1 for all accumulations where $dP/dz > 1$ and for cases in which particle peaks did or did not form. $dP/dz = 0^+$, particle number just begins to increase; $dP/dz = \max$, rate of particle number increase is maximum; $dP/dz = 0^-$, maximum number of particles; $dP/dz = \min$, particle number decreases at maximum rate.

	No. of times $Ri \leq 1$		
	$dP/dz > 1$ ($N = 54$)	$dP/dz > 1$ but not peak ($N = 24$)	Peak* ($N = 31$)
$dP/dz = 0^+$	41 (76%)	20 (83%)	23 (74%)
$dP/dz = \max$	40 (74%)	21 (87%)	20 (64%)
$dP/dz = 0^-$	37 (68%)	20 (83%)	17† (57%)
$dP/dz = \min$	24 (44%)	16 (67%)	9‡ (31%)

* Two peaks formed without dP/dz exceeding 1. Because of these and the edge effects, sum of columns 2 and 3 does not equal total in column 1.

† $N = 30$ and ‡ $N = 29$ because of uncertainties in Ri due to edge effects while filtering.

density data, several patterns emerge when changes in particle abundance are assessed relative to the Richardson number.

When dP/dz is compared with Ri in the upper 40 m (Figs. 4B,C and 5B,C), $Ri \leq 1$ and frequently < 0.5 when particle numbers were increasing, and in all but peak 2 of Fig. 4, Ri exceeded 4 at the particle maximum ($dP/dz = 0^-$). From this we infer that the water column was turbulent where particle numbers began to increase but that stratification had damped the turbulence by the depth at which particle numbers had reached their maximum.

With a few exceptions, the above pattern was dominant in abundance peaks. For example, peak 2 appears to have been caused by an intrusion, and Ri is < 1 throughout peaks 3 and 4 (Fig. 4). These latter two abundance peaks were barely significant. The dominant pattern also occurred in peak 5, Fig. 4, and peak 3, Fig. 5. In these two peaks, the derivative of particle abundance increases, decreases to near 0, and then increases again before going negative. This double peak in the derivative suggests that these large abundance peaks resulted from the merger of two smaller peaks. Interpreted this way, the pattern found in the upper 40 m is observed, with low Ri at the top of the peak and $Ri > 1$ as particle abundances reach their first maxima. The pattern is repeated in the second half of peak 3 (Fig. 5).

Table 4 summarizes the relationship of Ri to increases in particle abundance for all the appropriate profiles. Observations of Ri throughout each region in which particles accumulated ($dP/dz \geq 1$), not just where particle peaks occurred, indicate that mixing events were more likely where particles were increasing in number than where they were decreasing. Where particle abundances were increasing, Ri was ≤ 1 ~76% of the time (Table 4). There were fewer incidences of low values of Ri when the abundance of particles was greatest and even fewer when the abundance of particles decreased most rapidly. The trend

Table 5. Characteristics of particle peaks for which $Ri \leq 1$ near the top and > 1 below and of particle peaks that do not have these characteristics.

Criteria: $Ri \leq 1$ near top and > 1 below	
No. of peaks satisfying criteria	21
with halocline or halocline and thermocline in region of peak	12 (57%)
with thermocline alone in peak*	3 (14%)
associated with intrusions†	6 (29%)
No. of peaks not satisfying criteria	10
associated with intrusions	3 (30%)
in the upper mixed layer with $Ri \leq 1$	2 (20%)
in deeper water with $Ri \leq 1$ everywhere below intrusions with high shear but $Ri > 1$ in peak region	1 (10%)
for which a halocline and thermocline comprise the entire region of the peak; $Ri < 1$ above pycnocline but > 1 within it with $Ri < 1$ where peak has its maximum concentration	1 (10%)
	2 (20%)

* Three of the peaks have changes in velocity suggestive of intrusions.

† Four of the intrusions have changes in T and S and velocity; two have changes only in velocity.

was accentuated when peaks formed, with half as many low values of Ri in the bottom half of the peak as when peaks did not form. There were more instances of low Ri when peaks did not form.

Observations of Ri within particle peaks themselves confirmed that 77% of the actual particle peaks had values of $Ri \leq 1$ in the uppermost part of the peak (Table 3). The importance of stratification as well as mixing to peak formation is suggested by the fact that 68% of the particle peaks had values of $Ri \leq 1$ near the top of the peak but larger values below.

The importance of stable stratification and, in particular, salt stratification is highlighted by the fact that 57% of the peaks for which $Ri \leq 1$ at the top and larger below had either a halocline alone or a halocline and a thermocline below the mixing zone (Table 5). Only 14% had a thermocline alone, and 29% were associated with intrusions or high values of mean shear.

Of the peaks that did not follow the above pattern (Table 5), 30% were associated with intrusions. Only two peaks did not have values of $Ri \leq 1$ somewhere in their vertical extent.

Discussion

Aggregate abundances and distributions—Several previous studies have investigated the abundance and distribution of marine snow (aggregates > 0.5 mm) by means of imaging systems. Although all of these studies concentrated on abundance patterns below the mixed layer, several reported abundances in the upper 100 m. Gorsky et al. (1992) used a video system that imaged 0.4 liters of water and found 10–50 agg. liter⁻¹ in the upper 100 m

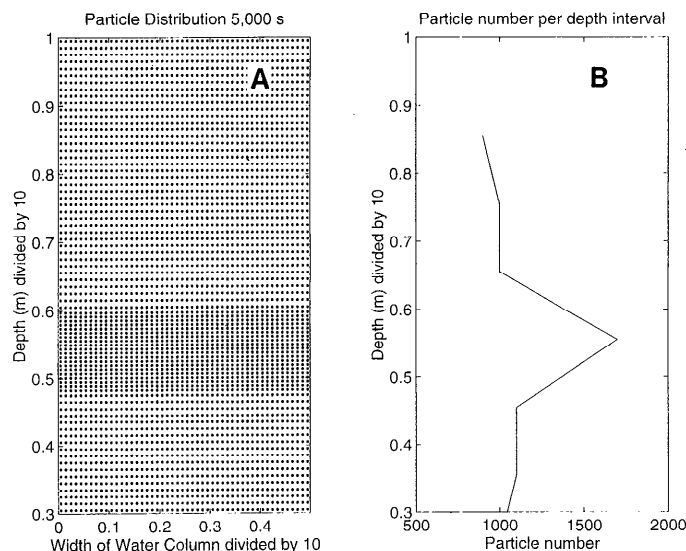


Fig. 7. Model of the effect of decreasing sinking rate on aggregate accumulation. A. Distribution of particles where sinking speeds decreased to 60% of initial speed below 0.6 m. B. Particle number at 1-m intervals. Model was run for 5,000 s in a 10- × 10-m grid where 10,000 particles were uniformly distributed initially. The time step was 25 s. Initial sinking speed of the particles was 35 m d⁻¹. Particles were continually introduced at the top at a rate that maintained the initial concentrations.

of the western Mediterranean—within the range of 6–110 agg. liter⁻¹ found at our coastal California stations. Walsh and Gardner (1992) reported total volumes of aggregates >0.5 mm in size in the upper 100 m of the Gulf of Mexico ranging from 10 to 30 mm³ liter⁻¹; they used a still-photography system imaging 8.3 liters of seawater. We observed a range of 11–350 mm³ liter⁻¹ with upper mixed layer means of 43 mm³ liter⁻¹. Photographic systems that image large volumes of seawater per frame (>600 liters) such as those of Honjo et al. (1984) or Asper et al. (1992) tend to report surface-water abundances of marine snow about 1 order of magnitude lower than ours, probably due to the lower resolution that is the result of imaging a large volume.

Mechanisms causing accumulation of aggregates—Regions with high abundances of marine snow were strongly associated with physical discontinuities in the water column. We hypothesize that these accumulations could have been caused by three mechanisms: reductions in aggregate sinking speeds as they settled into water with higher densities, interactions with the turbulent flow field, or intrusions.

Sinking speed could be reduced if the interstitial water or the mucus gels in flocs do not immediately equilibrate to the higher density of the surrounding water. To determine the likelihood of this mechanism, we assessed the percent reductions in sinking speed and increases in σ_t required for particle accumulations and examined the potential contribution of mucus to lowered sinking speeds.

In addition, we analyzed whether temperature and salinity are exchanged slowly enough within the interstitial water of aggregates for reduced sinking speeds to persist long enough to allow accumulations.

Low values of Ri suggest turbulent mixing in the water column; we used a random walk simulation to examine the consequences of mixing. We expected turbulence could increase flocculation rates, alter the distribution of aggregates, prolong the time flocs remain in suspension, and entrain water with greater numbers of particles from deeper depths.

Finding regions where marked changes in current speed and (or) direction (i.e. changes in shear) co-occur with hydrographic changes suggests that intrusions were important in causing accumulations at least 23% of the time. This topic was discussed above and is not developed further.

Hypothesis 1: Accumulation results from reduction of aggregate sinking speeds as aggregates settle into water of higher density—We investigated this hypothesis by examining a series of questions, each addressing a subset of the overall hypothesis.

What reductions in sinking speed are required to produce accumulations? To determine the reduction in sinking speed necessary for particles to accumulate at density discontinuities, we modeled the sinking of aggregates into a pycnocline by letting the initial sinking speed decrease as the aggregate passed a boundary. Below the boundary, sinking speeds were also reduced. The runs were performed for 5,000 s, the time required for aggregates sinking 35 m d⁻¹ to sink 2 m. We ran the model four times with reduced sinking speeds that were 90, 80, 60, and 30% of the initial value; aggregate numbers are increased 70% over those in the overlying water (Fig. 7)—an increase typical of those observed at our study sites. Particle numbers increased 20, 30, and 250% in the meter below the boundary when sinking speeds were 90, 80, and 30% of the initial speed at the discontinuity (not shown). Concentrations did not reach their maximum in the last run because particles with reduced sinking speeds did not have time to sink 1 m. Note that these distributions show increased abundances only where sinking speeds are reduced, not above the density discontinuity as found in nature (Table 1). When the analysis is performed over a period of several hours with a steady introduction of particles, the maximum number of aggregates per meter does not increase, but more of the stratified region has high abundances. These model results indicate accumulations can occur when sinking speeds are reduced by 20% or more.

What changes in aggregate excess density would be necessary to reduce sinking speeds sufficiently? The sinking speed (U) of a floc of marine snow is given by

$$U = (2g\Delta\rho V/\rho_f C_d A)^{1/2}.$$

$\Delta\rho$ is the excess density of the floc, V is aggregate volume, A is cross-sectional area perpendicular to the direction of sinking, ρ_f is ambient density, and C_d is the drag coefficient.

cient which ranges from 1 to 1,000, depending on Reynolds number (Alldredge and Gotschalk 1988). The above expression can be reduced to show the dependence of U on $\Delta\rho$ for a floc of a given size:

$$U = (k\Delta\rho)^{1/2}$$

where $k = 2gr/C_d\rho_f$ (r is radius). The reduction in sinking speed depends on the ratio of $\Delta\rho^{1/2}$ where the aggregate is formed to $\Delta\rho^{1/2}$ at the elevated density.

The $\Delta\rho$ of an aggregate comprised of a solid component and interstitial fluid as it sinks into water of higher density is

$$\Delta\rho = (\phi)\Delta\rho_s + (\eta)\Delta\rho_{fa}.$$

$\Delta\rho_s$ is the excess density of the solid fraction, $\Delta\rho_{fa}$ the excess density of the interstitial fluid, and η is the porosity and ϕ the solid volume fraction of the aggregate. Where the aggregate initially forms, the density of the interstitial fluid is the same as that of the surrounding fluid, and sinking speed only depends on the excess density of the solid fraction. However, as the particle sinks into denser fluid, $\Delta\rho_{fa}$ becomes negative and the sinking speed of the particle is reduced.

We solved the above equation for sinking speed using 0.01 and 0.06 g cm⁻³ for the excess density of the solid fraction and porosities of 99, 99.9, and 99.99%. Excess densities of the solid fraction were chosen to be similar to major components of marine snow, fecal pellets, and diatoms. Laboratory experiments determined the excess density of chaetognath fecal pellets to be 0.01 g cm⁻³ (Dilling and Alldredge 1993). This value is considerably lower than the excess density of 0.2 g cm⁻³ obtained for crustacean pellets by Komar et al. (1981) by indirect methods. Excess densities of living diatoms range from 0.01 to 0.03 g cm⁻³, whereas excess densities of senescent diatoms range from 0.04 to 0.08 g cm⁻³ (Eppley et al. 1967). Porosities of 99, 99.9, and 99.99% have been observed in flocs <3 mm, 2–10 mm, and 4–20 mm in diameter, respectively (Alldredge and Gotschalk 1988).

When aggregate excess density is 0.01 g cm⁻³ (Fig. 8A), flocs with porosities of 99.9% or greater rapidly decrease in sinking speed for increases in σ_t of <0.02. If this increase in σ_t occurs over 1 m, $N^2 = 2 \times 10^{-4}$ s⁻². The decrease in sinking speed with increase in σ_t is less for flocs whose porosity is 99%; however, an increase in σ_t of 0.04 would reduce sinking speed by 20%, just enough to create a significant peak in abundance.

For an aggregate excess density of 0.06 g cm⁻³ (Fig. 8B), only the most porous flocs would have large decreases in sinking speed with small changes in σ_t . Sinking speeds of flocs with $\eta = 99.9\%$ would decrease to 80% of their initial value for an increase in σ_t of 0.025. The least porous flocs would have such a small decrease in sinking speed that they would not be expected to accumulate with increases in density.

Flocs <1-mm diameter accounted for 90% or more of the aggregates in most of our aggregate peaks, and their porosity is 99% or less. These aggregates are more likely to be detrital marine snow, for which an excess density

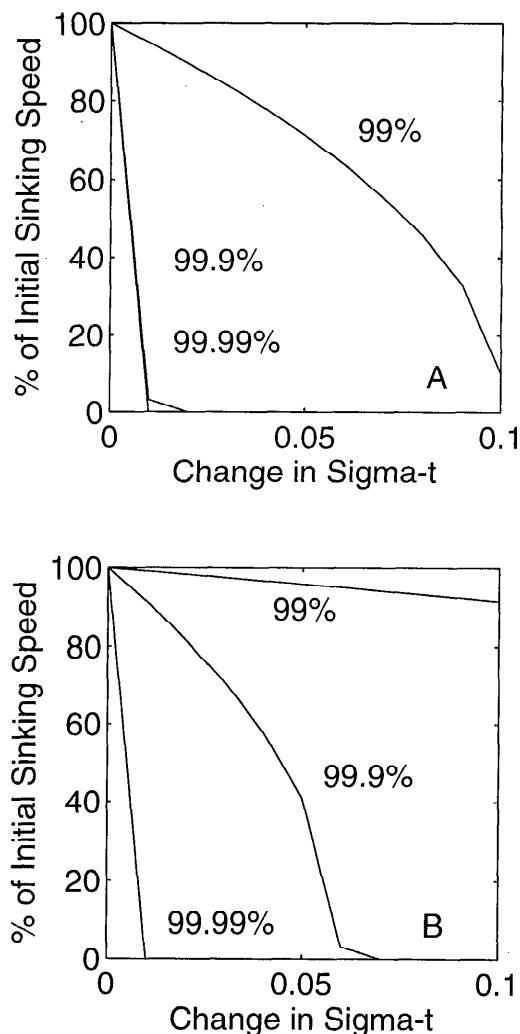


Fig. 8. Decrease in sinking speed for increases in σ_t for aggregates with porosities of 99, 99.9, and 99.99% assuming the density of the solid fraction was 0.01 g cm⁻³ (A) and 0.06 g cm⁻³ (B).

of 0.01 g cm⁻³ is a reasonable value. Consequently, these small particles are likely to be retained at density discontinuities, but only if changes in σ_t exceed 0.04. More porous flocs are likely to slow as they settle into denser water. However, for reductions in sinking speed to lead to accumulations of aggregates, the disequilibrium of interstitial water must persist for some period of time.

Mucus forms the matrix of most marine snow and is especially abundant in aggregates dominated by diatoms (Alldredge et al. 1993). If an aggregate contains mucus, excess density can be expressed as

$$\Delta\rho = (\phi)\Delta\rho_s + Q\Delta\rho_{fa},$$

assuming the interstitial water immediately equilibrates with ambient and where Q is the fraction of the aggregate comprised of mucus that has an initial density nearly identical to that of the water in which it was formed. We solved for U as described above for aggregates containing

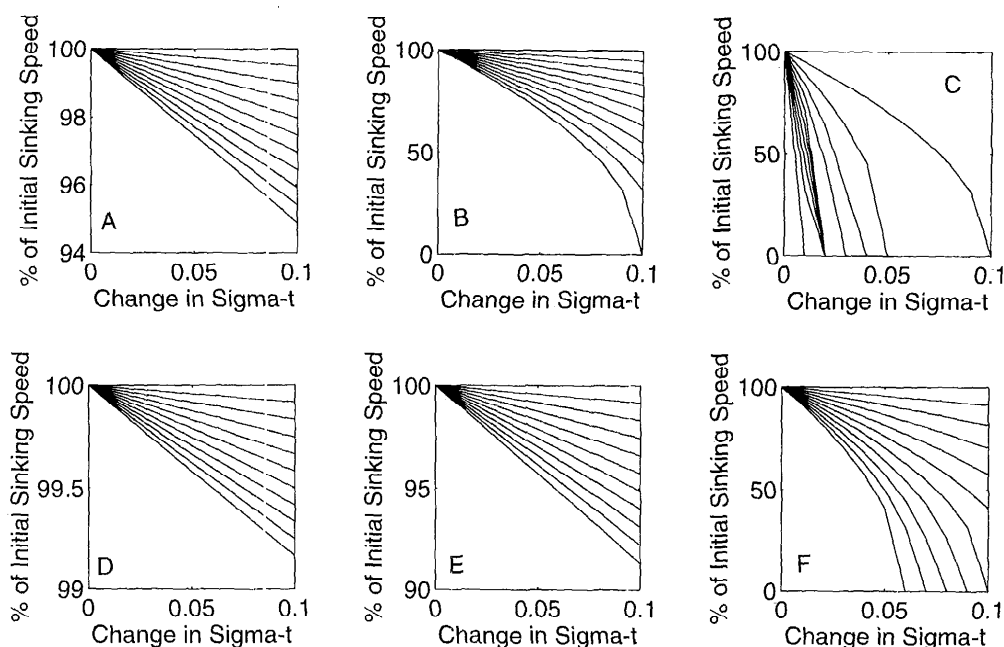


Fig. 9. Decrease in sinking speed for increase in σ_t for flocs containing mucus. A, B, and C. $\rho_s = 0.01 \text{ g cm}^{-3}$ and initial porosities without mucus are, respectively, 99, 99.9, and 99.99%. D, E, and F. $\rho_s = 0.06 \text{ g cm}^{-3}$ and initial porosities are 99, 99.9, and 99.99%. Axes are scaled for greatest resolution within each panel. Mucus contents range from 1%, uppermost curve, to 10%, lowest curve in each panel.

1–10% mucus. Because $\phi + \eta + Q = 1$ and ϕ is constant, mucus content of $>10\%$ would lead to calculated porosities lower than those determined from marine snow samples.

Figure 9 summarizes the effect of mucus content on the sinking of aggregates. For a mucus-containing aggregate with an initial porosity of 99%, sinking speed would be reduced at most by 5% for changes of σ_t at the upper end of the range observed in our study (Fig. 9A,D). High mucus content and large increases in σ_t are required before sinking speeds would decrease in flocs for which $\eta = 99.9\%$ and $\Delta\rho = 0.01 \text{ g cm}^{-3}$ (Fig. 9B); sinking speeds would decrease $<10\%$ if excess density was 0.06 g cm^{-3} (Fig. 9E). However, for highly porous flocs with $\Delta\rho = 0.01 \text{ g cm}^{-3}$, large reductions in sinking speed do occur as σ_t increases (Fig. 9C). If mucus content is high, settling speeds of highly porous flocs whose excess density is 0.06 g cm^{-3} could be reduced 80% by changes in σ_t of the magnitude we observed (Fig. 9F).

In summary, reductions in sinking speed due to disequilibrium of the density of mucus and surrounding water and sufficient to result in accumulations are likely for highly porous flocs and are most likely for those with an excess density of 0.01 g cm^{-3} .

How long will reduced sinking speeds persist? To determine whether the reduced sinking speeds of marine snow would persist long enough to allow accumulations, we investigated the time required for equilibration of the interstitial fluid of the aggregate with the surrounding water. We calculated the time for heat and salt to exchange by molecular diffusion within an aggregate and the time

for water to flow through a floc according to Stolzenbach (1993). If the exchange rate is fast, the aggregate will not slow as it enters denser water.

The time scale, t , for molecular diffusion of heat or salt within the floc is

$$t = r^2/2D$$

where the radius of the floc is $2r$ and D is the coefficient of molecular diffusivity. The relation is typically used to predict the spread of molecules from a point-source, and the final distribution is Gaussian with a width of $4r$ where r^2 is the variance (Fischer et al. 1979).

Figure 10 is a diagram of flow through a slightly permeable floc, assuming flow can be modeled based on a porous sphere. The time for pressure-driven flow to pass through the floc is $2r/U_t$, where

$$U_t = 3\kappa U/2r^2.$$

κ is permeability and U_t is the velocity of pressure-induced flow. The time for shear-driven flow to circulate through the boundary layer is $\theta r/U_s$, where θ in radians is the angle subtending the boundary layer, and U_s (the maximum velocity of flow driven by shear forces through a boundary layer of thickness $\sim \kappa^{1/2}$) is

$$U_s = 3\kappa^{1/2}U/2r.$$

Permeability depends on aggregate porosity and can be calculated from

$$\kappa = a_p^2[16\phi^{1.5}(1 + 56\phi^3)]^{-1}.$$

a_p is the characteristic radius of the particles comprising

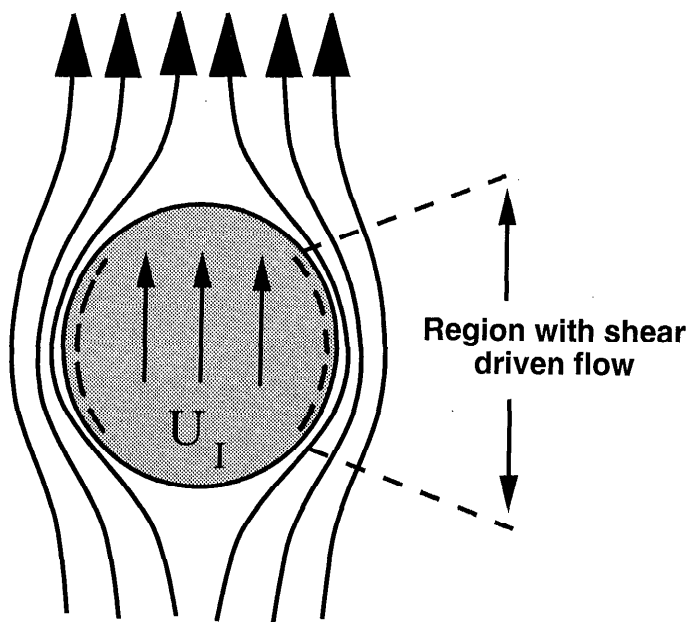


Fig. 10. Diagram of flow past a sinking aggregate (modified from Stolzenbach 1993). A pressure-driven flow penetrates most of the floc with velocity U_I , dependent on the permeability κ , radius r , and sinking rate of the floc. A shear-driven flow is generated near the boundary where streamlines converge. The velocity of this flow depends on the same factors and its thickness is $\sim 2\kappa^{1/2}$.

the aggregate, assumed to be $7\ \mu\text{m}$ for diatom flocs and $0.6\ \mu\text{m}$ for detrital marine snow (Stolzenbach 1993).

The parameter β , defined as $\beta = r/\kappa^{1/2}$, determines the applicability of the above model. When β is $\lesssim 2$, the external flow passes through the floc with little deflection of the flow. However, as β increases above 2, more and more of the flow will go around the floc instead of through it, and the two types of flows described above will be generated within the floc (Stolzenbach 1993).

Flow speeds were calculated as a function of radial position and angular position using the stream function for flocs of low permeability (Stolzenbach 1993, equation A3). These calculations were necessary to determine where shear flow was important and to more accurately assess boundary-layer thickness.

We modeled the sinking characteristics of two types of marine snow: compact aggregates composed primarily of detritus, fecal matter, and debris and larger porous flocs formed by chain-forming diatoms. Detrital marine snow is far more resistant to flow than are diatom flocs, as evidenced by β ranging from 10 to ~ 400 as opposed to from 7 to 23 (Figs. 11 and 12 axes). Shear-driven flow occurs in at most 20% of the volume of detrital marine snow and within 25–45% of the volume of diatom flocs (not shown).

Diffusion is much more rapid than either shear- or pressure-driven flow in detrital marine snow (Fig. 11), and since diffusion of heat takes $< 10\ \text{s}$ and is two orders of magnitude more rapid than diffusion of salt, the time for salinity to equilibrate determines how long an aggre-

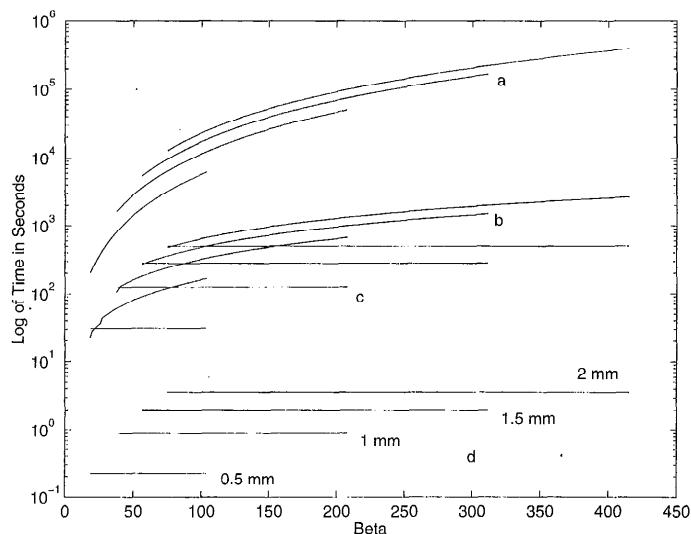


Fig. 11. Time for pressure-driven flow to pass through a floc of marine snow (a), shear-driven flow to circulate through the shear-driven boundary layer (b), salt to equilibrate by molecular diffusion (c), and heat to equilibrate by molecular diffusion (d). These times are plotted against $\beta = r/\kappa^{1/2}$, where r is radius and κ is permeability, which indicates the degree the external flow will be deflected around the floc; low values of β indicate lesser deflection. Radii of detrital marine snow modeled were 0.5, 1, 1.5, and 2 mm and ϕ ranged from 0.001 to 0.01 (Allredge and Gotschalk 1988). ϕ decreases with floc size, but we assumed that the above values applied to all sizes of flocs because ϕ varies by an order of magnitude for each floc size (Allredge and Gotschalk 1988). The four lines or curves within each group represent the four radii used in the calculations, with the lowest line or curve the results for 0.5 mm, the highest for 2 mm. Permeability decreases from left to right. Results are presented for sinking speeds of $35\ \text{m d}^{-1}$ and were similar for sinking speeds of 50 and $100\ \text{m d}^{-1}$.

gate of marine snow will have a slower speed as it sinks through water with greater density. Therefore, lower sinking rates are to be expected only when detrital marine snow sinks through a halocline. Salt will equilibrate in 30 s for detrital marine snow with a radius of 0.5 mm; however, for marine snow 2 mm in radius, equilibration will occur in $\sim 10\ \text{min}$.

The equilibration time of diatom flocs depends on the time for flow to penetrate through them. Again heat diffusion is rapid, but the time scales for pressure-driven and shear-induced flow are less than or equivalent to that for salt diffusion (Fig. 12) for all flow speeds. For the smallest, most permeable flocs, flow will penetrate rapidly. Once β exceeds 7, flocs equilibrate in $\sim 100\ \text{s}$. The larger, least permeable flocs will take up to 3 h to equilibrate. Flocs requiring at least a half hour to equilibrate were common at all three flow speeds. Again, because temperatures inside diatom flocs equilibrate rapidly, reductions in sinking rate are more likely as flocs sink into more saline waters.

We ran our model of particles sinking into a density gradient for 50, 100, and 500 s to determine whether these times were long enough for appreciable accumu-

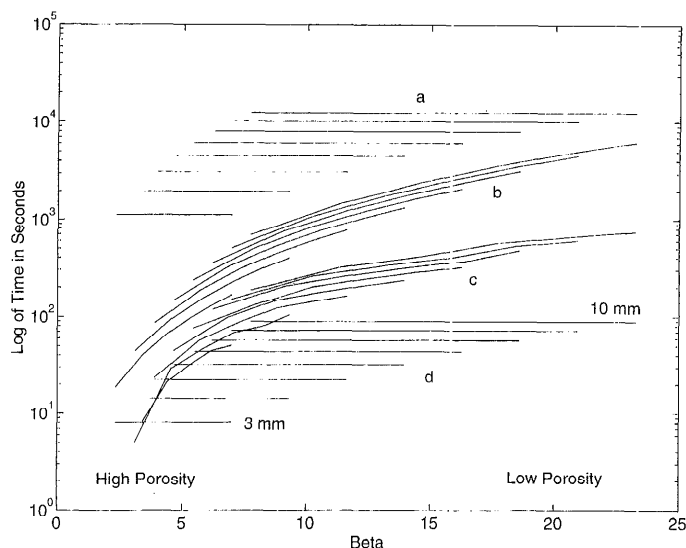


Fig. 12. As in Fig. 11, but for diatom flocs (note that a, b, and c are not in the same order as in Fig. 11). Time for salt to equilibrate by molecular diffusion (a), pressure-driven flow to pass through the floc (b), shear-driven flow to pass through the shear-generated boundary layer (c), and heat to equilibrate by molecular diffusion (d). The radii of diatom flocs ranged from 3 to 10 mm with ϕ ranging from 1.5 to 6.2×10^{-4} (Logan and Alldredge 1989). The lowermost line in group a corresponds to a radius of 3 mm, the uppermost to 10 mm.

lations to occur. When sinking speed was 60% of the initial value, the number of particles only increased 10% where particles slowed for these three time intervals. For a 70% reduction in sinking speed, numbers increased 10% after 50 and 100 s, and increased 20% after 500 s. Aggregates that equilibrate rapidly will not accumulate appreciably at density discontinuities.

Reductions in sinking rate may persist considerably longer if the aggregates contain appreciable gellike mucus. Because the diffusion coefficients of heat and salt within flocs as well as the mucus content are unknown, no analysis such as that for interstitial water can be done. However, the diffusion coefficients of heat and, in particular, salt within mucus are likely to be much smaller than in water, and reduced sinking rates are expected for much longer times. Again, reduction in sinking speeds due to slow equilibrium of mucus is likely in highly porous flocs, especially those comprised of living diatom cells.

Were observed density gradients large enough to explain accumulations by reduced sinking speeds? Although the most porous flocs will be retained at modest density discontinuities for periods up to several hours by slow equilibrium of either their interstitial fluid or mucus, increases in σ_t of at least 0.04 are required for small flocs of low porosity to accumulate and of 0.025 for flocs with $\Delta\rho = 0.06 \text{ g cm}^{-3}$ and $\eta = 99.9\%$.

Half the profiles taken had at least one density discontinuity with $N^2 > 4 \times 10^{-4} \text{ s}^{-2}$, a value equivalent to $\Delta\sigma_t \text{ m}^{-1}$ of 0.04, and one profile had $N^2 = 35 \times 10^{-4} \text{ s}^{-2}$. These large Brunt-Väisälä frequencies indicate that

in some cases aggregates with low to moderate porosity will be retained at discontinuities. However, marine snow with a sinking speed of 35 m d^{-1} would sink 1 m in 2,500 s, and many small flocs and a number of larger ones will equilibrate in a shorter time. Consequently, more abrupt changes in density may be necessary for accumulations. A density profile taken with the fine-structure profiler showed that rapid density increases over small depth intervals do sometimes occur; for example, we observed increases of σ_t of $\sim 0.025 \text{ kg m}^{-3}$ in 0.15 m three times in a 5-m section of the pycnocline as well as several increases of $\sim 0.015 \text{ kg m}^{-3}$ over distances $< 0.1 \text{ m}$. These increases may still be too small for accumulation of flocs with low porosity, but moderate to highly porous flocs will accumulate and some may become neutrally or negatively buoyant. Where N^2 is $< 4 \times 10^{-4} \text{ s}^{-2}$, flocs may accumulate, but the number will be less due to the smaller changes in σ_t .

Since salinity rather than heat is the critical factor for reduction of sinking speeds, density increases must in part be due to salinity increases for aggregates to be retained due to slow equilibration of interstitial water. The mean salinity change in the water column where aggregate numbers increased was $0.015 \pm 0.014\text{‰ m}^{-1}$. Only 48% of the accumulations were associated with increases in salinity. The contribution of salinity to each change in density can be calculated from $\rho = B \Delta T + \alpha \Delta S$, where B (the thermal coefficient of expansion) is -0.21 , and α (the coefficient of expansion due to salinity) is 0.77 for the temperature and salinity ranges we observed (Fofonoff and Millard 1983). When we used the mean value for salinity change and $N^2 = 1.25 \times 10^{-4}$, 88.4% of the density change was due to salinity. When $N^2 = 2.5 \times 10^{-4}$, half the density change was due to salinity. As the contribution of salinity decreases, larger changes in σ_t are required for reductions in aggregate sinking speed. For instance, salinity accounted for only 24% of the pronounced changes in density measured by the fine-structure CTD discussed above, making these sites less likely to retain low to moderately porous flocs.

Hypothesis 2: Accumulations result from interactions with the turbulent flow field—Turbulence may produce increased aggregate abundance through two mechanisms: direct accumulation or increased rate of aggregate formation.

For direct accumulation, we used a random walk technique (Patterson 1991) to simulate the distributions of flocs within a turbulent zone. In this technique, particles are allowed to settle in a flow field with random velocity fluctuations; particle velocity is the sum of sinking speed and a turbulent velocity. The locations of individual flocs are computed over a time step, $\Delta t = l_t/u_t$, which we chose to give a characteristic turbulent length scale l_t of 0.1 m. We ran two cases, one in which the turbulent velocity scale (u_t) was equal to the sinking speed (U) of aggregates and one in which u_t was 10 times higher than U . The turbulent velocity was $u_t \cos\theta$ in the x -direction and $u_t \sin\theta$ in the y -direction where the angles are selected randomly.

The simulations illustrated are for the case of a tur-

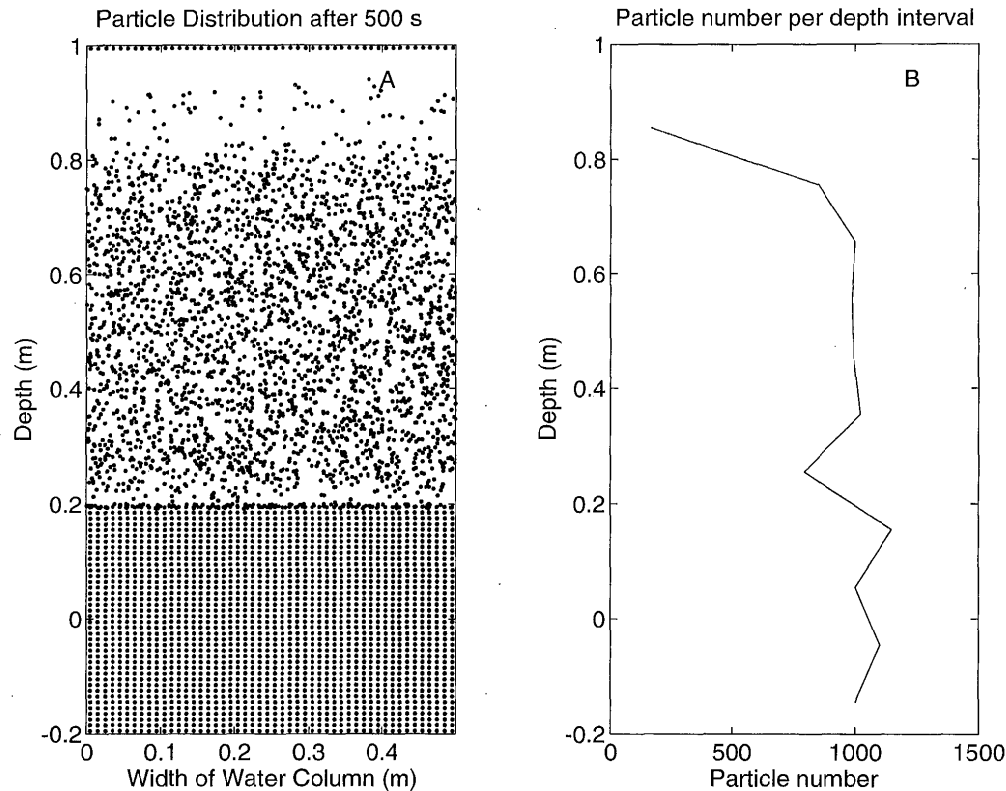


Fig. 13. Random walk simulation of particle distributions in a turbulent flow field. Initially, 10,000 particles were uniformly distributed in a 1×1 -m grid. Flow was turbulent only in the upper 0.6 m of the grid. The model was run for 500 s with time scale $l_t/u_t = 25$ s. u_t equaled a particle sinking speed of 0.0004 m s^{-1} (35 m d^{-1}). Newly introduced particles form a horizontal line at 1-m depth. A. Distribution of particles in 0.5-m-wide water column. B. Particle distribution with depth calculated in 0.1-m intervals.

bulent layer bounded by nonturbulent layers. A particle leaving at the side boundaries was replaced with one entering at the same point. The upper and lower boundaries were reflective, but we allowed the turbulent patch to grow at a rate dependent on the turbulent Richardson number (Imberger and Patterson 1990, equation 4.28). The patch grew, thereby entraining fluid within 0.2 m of the upper and lower boundary within 500 s. The aggregates were initially uniformly distributed in a 1-m^2 grid, but once the simulation was started, aggregates were added at 1-m depth at a rate that maintained the initial concentrations. The sinking speed of the flocs was 35 m d^{-1} , equivalent to 0.0004 m s^{-1} . If we use the relation $\epsilon = u_t^3/l_t$ (where ϵ is energy dissipation rate), $\epsilon = 6.4 \times 10^{-7} \text{ m}^2 \text{ s}^{-3}$ for u_t 10 times higher than U , and $\epsilon = 6.4 \times 10^{-10} \text{ m}^2 \text{ s}^{-3}$ for u_t equivalent to U . The former value of ϵ is representative of moderately turbulent waters; the latter is typically not considered turbulent, but in a simulation such as this will still describe the combined effects of sinking in a field with random velocity fluctuations.

We present results obtained after 500 s—the period individual overturns might persist in coastal waters and the time for particles to sink 0.2 m. A comparison of Figs. 13 and 14 shows the dramatic increase in particle number at the lower boundary between laminar and turbulent flow

when u_t is 10 times larger than U . For both cases, the turbulence brought particles into closer proximity, where the probability of aggregation is increased.

Although a population of particles will be kept in suspension for a longer time when turbulent velocities exceed particle sinking speeds by a factor of ~ 10 , more particles were lost from the turbulent layer in this short run where turbulence was strongest. However, the more energetic turbulence caused greater dispersion and more upward movement of particles. For example, when $u_t = U$, particles initially in the upper 0.2 m settled out of that zone (Fig. 13), whereas when $u_t = 10U$, particles were mixed upward into the newly entrained waters (Fig. 14). When we ran the simulation for the time for particles to sink 1 m, we did obtain the expected result: $<1\%$ of the particles remained in the turbulent layer when $U = u_t$, but $\sim 10\%$ of the population remained in the turbulent layer when $U = 0.1u_t$.

In coastal waters below the wind-mixed layer with stratification and shears comparable to those we observed, Yamazaki and Osborn (1993) obtained values of ϵ ranging from 5×10^{-10} to $5 \times 10^{-7} \text{ m}^2 \text{ s}^{-3}$, with highest values of ϵ when Ri was less than a critical value. Comparable values have been observed in stratified waters with overturns and in the mixed layer when windspeeds

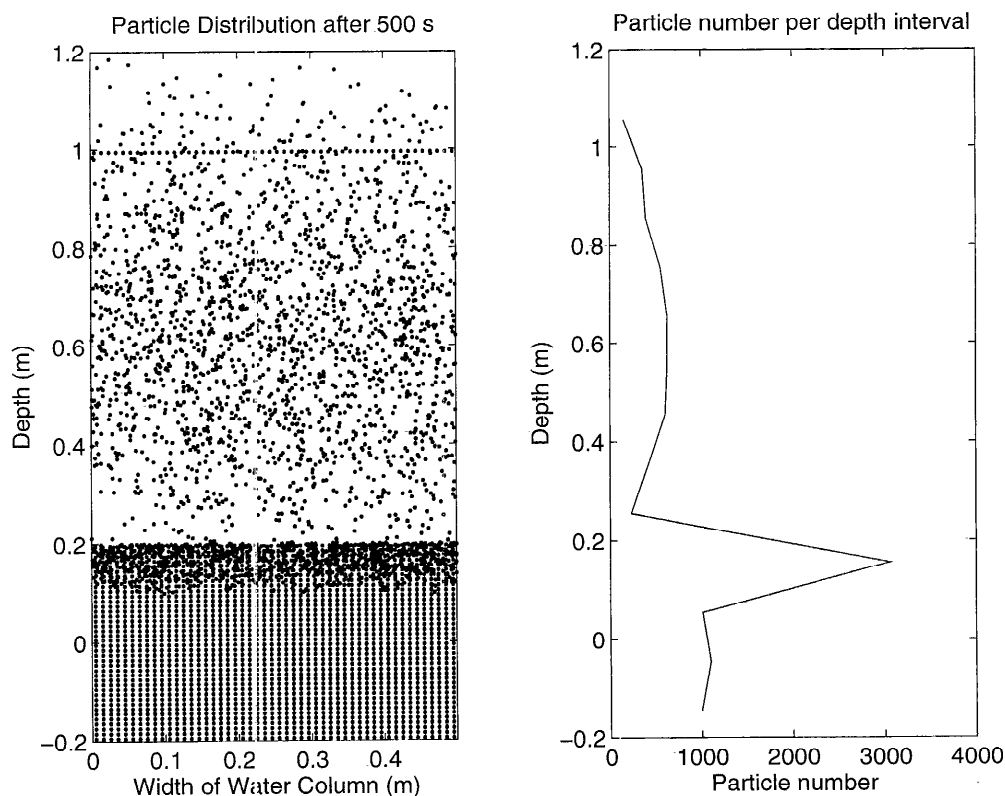


Fig. 14. As in Fig. 13, but u_t was 10 times larger than particle sinking speed of 0.0004 m s^{-1} .

are $< 7 \text{ m s}^{-1}$ (Hebert et al. 1991; Dewey and Moun 1990; MacIntyre 1993). Near the air–water interface, ε can be much higher, with maximum observed values of $10^{-4} \text{ m}^2 \text{ s}^{-3}$ (Brainerd and Gregg 1993; Agrawal et al. 1992). We expect that low to moderate values of ε comparable to those observed by Yamazaki and Osborn (1993) occurred during our study and that where $\text{Ri} \leq 1$, turbulent velocities could have been at least 10 times higher than aggregate sinking rates. We infer that turbulence in the pycnocline altered the distribution of marine snow and caused localized increases in the number of aggregates. Turbulence at low intensities was likely to prolong the residence time of diatoms and other components of marine snow with sinking speeds of $\sim 1 \text{ m d}^{-1}$, but persistent, moderate turbulent intensities would be required to maintain appreciable quantities of marine snow in suspension. Because 80–90% of the aggregates in accumulations are $< 1 \text{ mm}$ in size, turbulence may be of major importance in causing their accumulations.

We recognize that we have invoked a simple model of a complex flow which has a spectrum of eddy sizes and velocities, but we use it to indicate the potential for turbulent flows to cause localized abundances. Similar accumulations of particles, but over larger depth intervals, have been observed at the base of the mixed layer in more complex models of mixing layers (Woods and Onken 1982).

In addition, for those highly porous particles whose sinking speeds were significantly reduced at a density dis-

continuity, turbulence at the discontinuity will mix these flocs into the overlying water. Such resuspension events may be one reason for elevated concentrations of aggregates above density discontinuities.

The rate of aggregate formation will increase with increases in magnitude of the small-scale velocity gradients [$\gamma = (\varepsilon/\nu)^{1/2}$] due to the turbulence. These small-scale shears increase the rate of particle collisions but at higher turbulence intensities can deform aggregates, leading to disaggregation (Aldredge et al. 1990). Local velocity gradients span four orders of magnitude for the rates of energy dissipation found in upper mixed layers and pycnoclines. If typical values of ε below the wind-mixed layer at our study sites were 10^{-7} – $10^{-10} \text{ m}^2 \text{ s}^{-3}$ as discussed above, γ would have ranged from 0.32 to 0.01 s^{-1} . The maximum mean shears we observed equaled γ at the lowest dissipation rates, illustrating that turbulent motions can significantly increase the rate of aggregate formation. Because ε increases by 1–2 orders of magnitude as Ri drops below critical levels (Yamazaki and Osborn 1993; Peters et al. 1991), enhanced mixing rates, collisions between particles, and flocculation of TEP (transparent exopolymer particles whose scavenging of particles such as diatoms leads to floc formation, Passow et al. 1994) are expected where we observed low values of Ri . That we found $\text{Ri} \leq 1$ at the depths at which 76% of all particle accumulations initiated (Table 4) supports the argument that enhanced flocculation led to increases in abundance of particles $> 500 \mu\text{m}$. However, except under

bloom conditions, the time scale for doubling the number of particles due to flocculation is generally >1 d (Bruce Logan pers. comm.). Consequently, whereas flocculation contributes to the formation of aggregates, it is a more important mechanism for their accumulation on time scales of a day.

Importance of turbulence and reduced sinking speeds in causing accumulations—Our analysis indicates that small aggregates of low porosity accumulate because of turbulent mixing. Their sinking rates are not reduced sufficiently for the increases in density we observed, and they equilibrate too rapidly to accumulate because of slow equilibration of interstitial water. In contrast, larger, more porous flocs accumulate because their sinking rates are slowed as they encounter water of higher density, either because they contain mucus or because of slow equilibration of interstitial water. However, away from the surface zone where wind stirs the water and heat losses cause instabilities, turbulent mixing events only persist for time scales of π/N (MacIntyre 1993)—about 500 s in these coastal waters—and occur up to 30% of the time (Thorpe 1977). The low frequency and duration of these mixing events makes us skeptical that only one mechanism explains the accumulation of the smaller aggregates. A simple explanation could be that the density of the solid fraction is less than we have assumed. Alternatively, a dynamic situation may prevail. Over a period of an hour, there could be several turbulent events at or just above density discontinuities, leading to re-entrainment of flocs into the overlying water. If turbulent intensities are high enough, some of the most porous flocs may disaggregate, increasing the number of smaller flocs above and below the discontinuity. Rates of flocculation would also increase due to both the higher rates of shear and the high accumulations of small flocs caused by turbulence at the discontinuity. Because turbulent events can occur wherever shears are high relative to stratification, these mixing events can occur where waters are less stratified above a pycnocline and at or just above the many density discontinuities in the pycnocline. Small-scale mixing events in the pycnocline may explain the high abundance of small flocs in this region.

Persistence and ecological significance of layering of marine snow—We do not know how long the accumulations of aggregates we observed persisted, whether for only half an hour, for several hours, or for days. Results from the model of particle sinking suggest time scales of half hours to hours to obtain the magnitude of increases in particle number we observed at the discontinuities themselves. While the random walk simulation of aggregates in a turbulent flow field shows that high accumulations can occur rapidly, multiple mixing events are probably required to explain accumulations over larger depth intervals.

The persistence of layers of marine snow for hours to days is highly significant to the ecology of the ocean. Associated with these layers would be aggregate consum-

ers, larvae, euphausiids and copepods, and attached microorganisms, for whom nourishment would be plentiful while the accumulations persisted. Swimming plankton could also accumulate. Within these layers, the chemistry and optical properties of the surrounding seawater could be altered. Rapid solubilization of particles by attached bacteria (Smith et al. 1992), diffusion of ammonium enriched in large aggregates (Shanks and Trent 1979), or localized depletions of oxygen known to be associated with marine snow (Alldredge and Cohen 1987) may increase the localized levels of nutrients and dissolved organic matter available for free-living microorganisms or provide vertical layers of low oxygen.

Persistence of accumulations for periods of hours to days will also result in greater loss of aggregates to decomposition, solubilization, and consumption and reduce the magnitude of sinking material. The resulting changes in the depth-specific magnitude of particulate flux would alter the cycling of carbon and nutrients and the rates of scavenging of trace metals in the upper waters of the ocean. Further efforts to understand the mechanisms causing accumulation of smaller flocs, in particular the role of turbulence in maintaining or breaking up accumulations, and time-series studies of the accumulations and their associated communities will enable us to assess the persistence of accumulations of marine snow and to quantify their overall ecological importance.

References

- AGRAWAL, Y. C., AND OTHERS. 1992. Enhanced dissipation of kinetic energy beneath surface waves. *Nature* **359**: 219–220.
- ALLDREDGE, A. L. 1991. In situ collection and laboratory analysis of marine snow and large fecal pellets, p. 43–46. *In* Marine particles: Analysis and characterization. Geophys. Monogr. 63. AGU.
- , AND Y. COHEN. 1987. Can microscale patches persist in the sea? Microelectrode study of marine snow, fecal pellets. *Science* **235**: 689–691.
- , AND C. GOTSCHALK. 1988. In situ settling behavior of marine snow. *Limnol. Oceanogr.* **33**: 339–351.
- , ———, AND S. MACINTYRE. 1987. Evidence for sustained residence of macrocrustacean fecal pellets in surface waters off southern California. *Deep-Sea Res.* **34**: 1641–1652.
- , T. C. GRANATA, C. C. GOTSCHALK, AND T. D. DICKEY. 1990. The physical strength of marine snow and its implications for particle disaggregation in the ocean. *Limnol. Oceanogr.* **35**: 1415–1428.
- , U. PASSOW, AND B. E. LOGAN. 1993. The abundance and significance of a class of large, transparent organic particles in the ocean. *Deep-Sea Res.* **40**: 1131–1140.
- , AND M. W. SILVER. 1988. Characteristics, dynamics and significance of marine snow. *Prog. Oceanogr.* **20**: 41–82.
- ASPER, V. 1987. Measuring the flux and sinking speed of marine snow aggregates. *Deep-Sea Res.* **34**: 1–17.
- , S. HONJO, AND T. H. ORSI. 1992. Distribution and transport of marine snow aggregates in the Panama Basin. *Deep-Sea Res.* **39**: 939–952.
- BRAINERD, K. E., AND M. C. GREGG. 1993. Diurnal restrati-

- fication and turbulence in the oceanic surface mixed layer. 1. Observations. *J. Geophys. Res.* **98**: 22,645–22,656.
- CARR, M.-E., N. S. OAKEY, B. JONES, AND M. R. LEWIS. 1992. Hydrographic patterns and vertical mixing in the equatorial Pacific along 150° W. *J. Geophys. Res.* **97**: 611–626.
- DAVIS, D. L., AND C. H. PILSKALN. 1993. Measurements with underwater video: Camera field width calibration and structured lighting. *Mar. Technol. Soc. J.* **26**: 13–19.
- DEBOOR, C. 1978. A practical guide to splines. Springer.
- DEWEY, R. K., AND J. N. MOUM. 1990. Enhancement of fronts by vertical mixing. *J. Geophys. Res.* **95**: 9433–9445.
- DILLING, L., AND A. L. ALLDREDGE. 1993. Can chaetognath fecal pellets contribute significantly to carbon flux? *Mar. Ecol. Prog. Ser.* **92**: 51–58.
- EPPLEY, R. W., R. W. HOLMES, AND J. D. H. STRICKLAND. 1967. Sinking rates of marine phytoplankton measured with a fluorometer. *J. Exp. Mar. Biol. Ecol.* **1**: 191–208.
- ERIKSEN, C. C. 1978. Measurements and models of fine structure, internal gravity waves, and wave breaking in the deep ocean. *J. Geophys. Res.* **83**: 2989–3009.
- FISCHER, H. B., E. J. LIST, R. C. Y. KOH, J. IMBERGER, AND N. H. BROOKS. 1979. Mixing in inland and coastal waters. Academic.
- FOFONOFF, N. P., AND R. C. MILLARD, JR. 1983. Algorithms for computation of fundamental properties of seawater. UNESCO Tech. Pap. Mar. Sci. 44.
- FOWLER, S. W., AND G. A. KNAUER. 1936. Role of large particles in the transport of elements and organic compounds through the oceanic water column. *Prog. Oceanogr.* **16**: 147–194.
- FOZDAR, F. M., G. J. PARKER, AND J. IMBERGER. 1985. Matching temperature and conductivity response characteristics. *J. Phys. Oceanogr.* **15**: 1557–1569.
- GARDNER, W. D., AND I. D. WALSH. 1990. Distribution of macroaggregates and fine-grained particles across a continental margin and their potential role in fluxes. *Deep-Sea Res.* **37**: 401–411.
- GORSKY, G., AND OTHERS. 1992. Vertical distribution of suspended aggregates determined by a new video profiler. *Ann. Inst. Oceanogr.* **68**: 1–7.
- GREGG, M. C., D. P. WINKEL, AND T. B. SANFORD. 1993. Varieties of fully resolved spectra of vertical shear. *J. Phys. Oceanogr.* **23**: 124–141.
- HEBERT, D., AND OTHERS. 1991. The role of the turbulent stress divergence in the equatorial Pacific zonal momentum balance. *J. Geophys. Res.* **96**: 7127–7136.
- HONJO, S., K. W. DOHERTY, Y. C. AGRAWAL, AND V. L. ASPER. 1984. Direct optical assessment of large amorphous aggregates (marine snow) in the deep ocean. *Deep-Sea Res.* **31**: 67–76.
- IMBERGER, J. 1985. The diurnal mixed layer. *Limnol. Oceanogr.* **30**: 737–770.
- , AND J. C. PATTERSON. 1990. Physical limnology. *Adv. Appl. Mech.* **27**: 303–475.
- ITSWEIRE, E. C., T. R. OSBORN, AND T. P. STANTON. 1989. Horizontal distribution and characteristics of shear layers in the seasonal thermocline. *J. Phys. Oceanogr.* **19**: 301–320.
- KOMAR, P. D., A. P. MORSE, L. F. SMALL, AND S. W. FOWLER. 1981. An analysis of sinking rates of natural copepod and euphausiid fecal pellets. *Limnol. Oceanogr.* **26**: 172–180.
- KUNDU, P. K., AND R. C. BEARDSLEY. 1991. Evidence of a critical Richardson number in moored measurements during the upwelling season off northern California. *J. Geophys. Res.* **96**: 4855–4868.
- LOGAN, B. E., AND A. L. ALLDREDGE. 1989. The increased potential for nutrient uptake by flocculating diatoms. *Mar. Biol.* **101**: 443–450.
- MACINTYRE, S. 1993. Vertical mixing in a shallow, eutrophic lake: Possible consequences for the light climate of phytoplankton. *Limnol. Oceanogr.* **38**: 798–817.
- MOUM, J. N. 1990. The quest for K_p —preliminary results from direct measurements of turbulent fluxes in the ocean. *J. Phys. Oceanogr.* **20**: 1980–1984.
- PADMAN, L., AND T. M. DILLON. 1991. Turbulent mixing near the Yermak Plateau during the coordinated eastern Arctic experiment. *J. Geophys. Res.* **96**: 4769–4782.
- , AND I. S. F. JONES. 1985. Richardson number statistics in the seasonal thermocline. *J. Phys. Oceanogr.* **15**: 844–854.
- , M. LEVINE, T. DILLON, J. MORISON, AND R. PINKEL. 1990. Hydrography and microstructure of an Arctic cyclonic eddy. *J. Geophys. Res.* **95**: 9411–9420.
- PASSOW, U., A. L. ALLDREDGE, AND B. E. LOGAN. 1994. The role of particulate carbohydrate exudates in the flocculation of diatom blooms. *Deep-Sea Res.* **41**: 335–357.
- PATTERSON, J. C. 1983. General derivative approximations for finite difference schemes. *Int. J. Num. Meth. Eng.* **19**: 1235–1241.
- . 1991. Modelling the effects of motion on primary production in the mixed layer of lakes. *Aquat. Sci.* **53**: 218–238.
- PETERS, H., M. C. GREGG, AND T. B. SANFORD. 1991. Equatorial and off-equatorial fine-scale and large scale shear variability at 140°W. *J. Geophys. Res.* **96**: 16,913–16,928.
- , AND J. M. TOOLE. 1989. Meridional variability of turbulence through the equatorial undercurrent. *J. Geophys. Res.* **94**: 18,003–18,009.
- SHANKS, A. L., AND J. D. TRENT. 1979. Marine snow: Microscale nutrient patches. *Limnol. Oceanogr.* **24**: 850–854.
- SMITH, D. C., M. SIMON, A. L. ALLDREDGE, AND F. AZAM. 1992. Intense hydrolytic enzyme activity on marine aggregates and implications for rapid dissolution. *Nature* **359**: 139–142.
- STOLZENBACH, K. D. 1993. Scavenging of small particles by fast-sinking porous aggregates. *Deep-Sea Res.* **40**: 359–369.
- THORPE, S. A. 1968. A method of producing a shear flow in a stratified fluid. *J. Fluid Mech.* **32**: 693–704.
- . 1971. Experiments on the instability of stratified shear flows: Miscible fluids. *J. Fluid Mech.* **46**: 299–319.
- . 1977. Turbulence and mixing in a Scottish loch. *Phil. Trans. R. Soc. Lond. Ser. A* **286**: 125–181.
- WALSH, I. D., AND W. D. GARDNER. 1992. A comparison of aggregate profiles with sediment trap fluxes. *Deep-Sea Res.* **39**: 1817–1834.
- WELLER, R. A., AND OTHERS. 1991. Forced ocean response during the frontal air-sea interaction experiment. *J. Geophys. Res.* **96**: 8611–8638.
- WOODS, J. D., AND R. ONKEN. 1982. Diurnal variation and primary production in the ocean—preliminary results of a Lagrangian ensemble model. *J. Plankton Res.* **4**: 735–756.
- WIJSEKERA, H. W., AND T. M. DILLON. 1991. Internal waves and mixing in the upper equatorial Pacific Ocean. *J. Geophys. Res.* **96**: 7115–7125.
- YAMAZAKI, H., AND T. OSBORN. 1993. Direct estimation of heat flux in a seasonal thermocline. *J. Phys. Oceanogr.* **23**: 503–516.

Submitted: 24 March 1994

Accepted: 4 October 1994

Amended: 6 December 1994